united nations
educational, scientific
and cultural
organization

international atomic
energy agency

the
abdus salam
international centre for theoretical physics

SMR 1331/24

AUTUMN COLLEGE ON PLASMA PHYSICS

8 October - 2 November 2001

Solitary Waves, Radiation and Wave-Particle Interactions

Robert L. Lysak
University of Minnesota, U.S.A.

These are preliminary lecture notes, intended only for distribution to participants.

Ph.D thesis J.M Kindel, UCLA, 1970

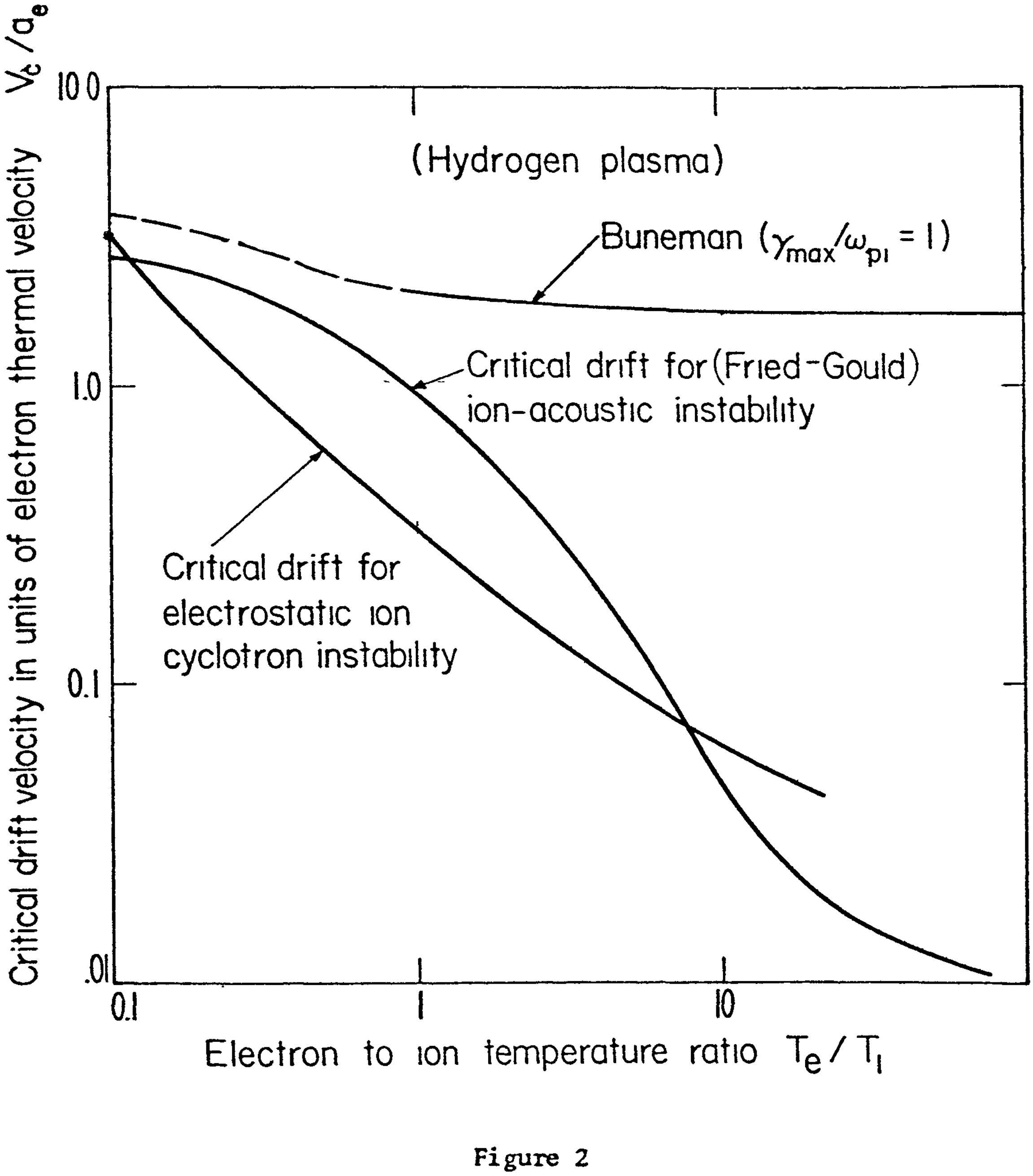

Figure 2

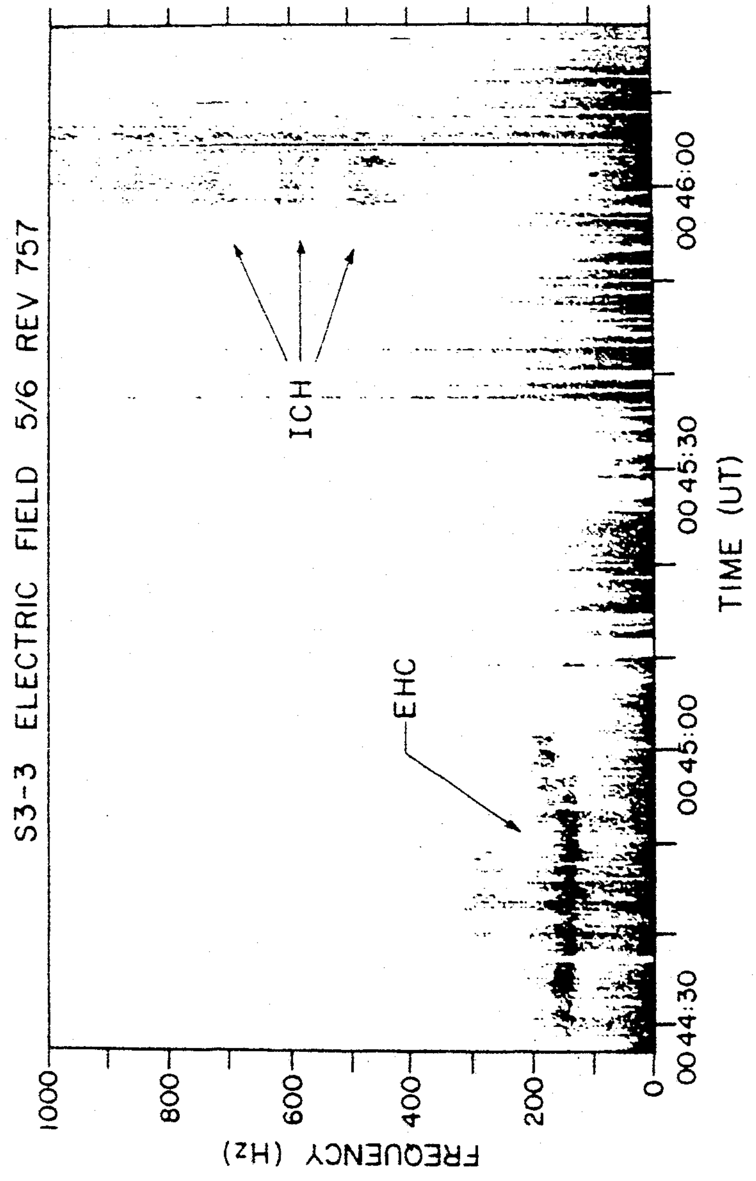
S3-3 ELECTRIC FIELD 5/6 REV 757
EHC
ICH
FREQUENCY (Hz)
1000
800
600
400
200
0
00 44:30
00 45:00
00 45:30
00 46:00
TIME (UT)

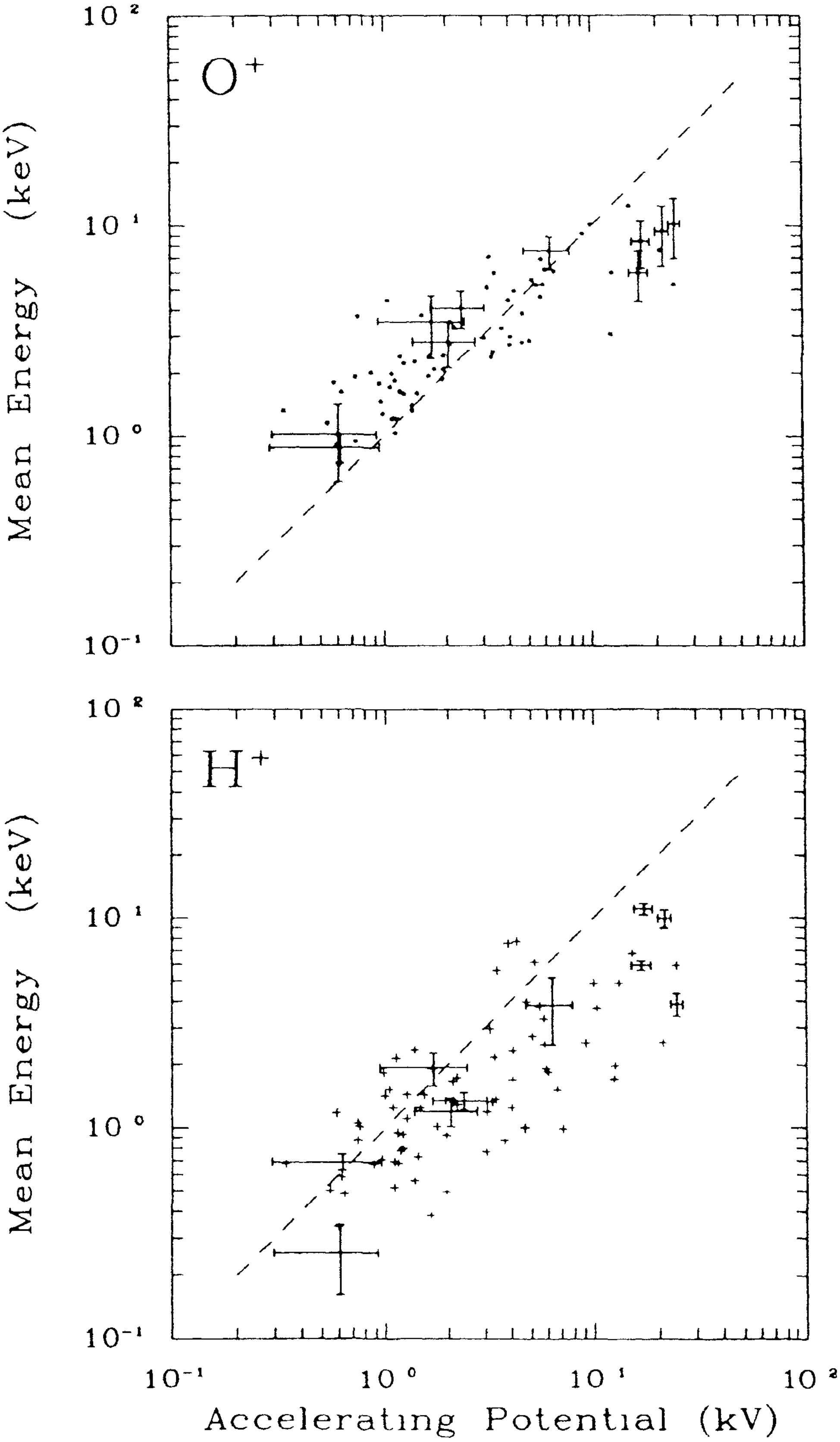
O+
H+
Mean Energy (keV)
Mean Energy (keV)
10^2
10^1
10^0
10^-1
Accelerating Potential (kV)

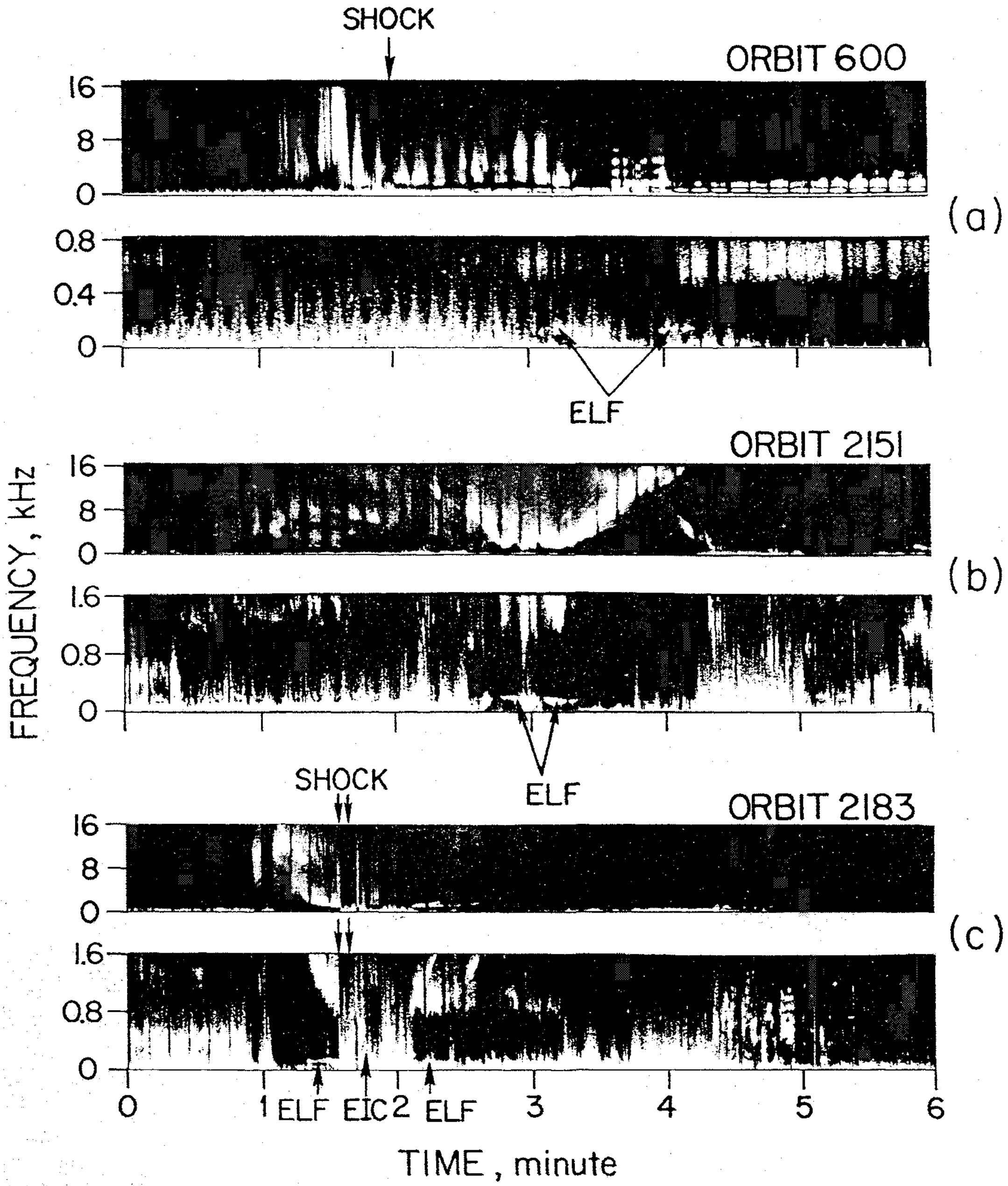

Fig. 3. Frequency-time spectrograms of narrow-banded ELF waves obtained at altitudes between 2000 and 4000 km.

time. This event had an ion beam in the energy range up to 3.9 keV and one of the largest electron fluxes ($\sim 5 \times 10^8$ el cm^{-2} sr^{-1} s^{-1} keV^{-1}) in the 1.5–5 keV range of any of the ELF events.

Figure 5 shows more detailed views of the ELF waveforms for one of the electric field components. The plotted data were produced by averaging, 40 points at a time, broadband data originally digitized at 44000 words/s from the antenna that was approximately in the north-south direction. Thus there were 1100 pts/s plotted in Figure 5 and some aliasing from higher frequencies occurs. Power spectra for the data segments in Figure 5 are shown in Figure 6. The frequency of ELF waves and of the local hydrogen cyclotron frequency (f_H) are marked. At higher frequencies, the usual VLF spectrum, with a sharp cutoff at the lower hybrid frequency, is evident. The ELF spectrum is usually narrow ($\Delta\omega / \omega < 0.2$ at half max), though both Figures 6*a* and 6*d* are somewhat wider. There is, in some cases, power extending up to the hydrogen cyclotron frequency. Figure 6*a* is particularly unusual, since there is an additional peak at 25 Hz which is approximately half the frequency of the main peak at 50 Hz. The 25 Hz peak lasts only a brief time compared to the 50 Hz peak. Though unusual, this is not a unique example. Note that the lowest frequency example in Figure 1 also has a harmonic relation to a higher frequency.

The polarization of the electric field can be determined because the S3-3 satellite measured all three components of the electric field. The electric field is polarized perpendicular to the magnetic field to the 10% accuracy to which the three components of the electric field can be easily

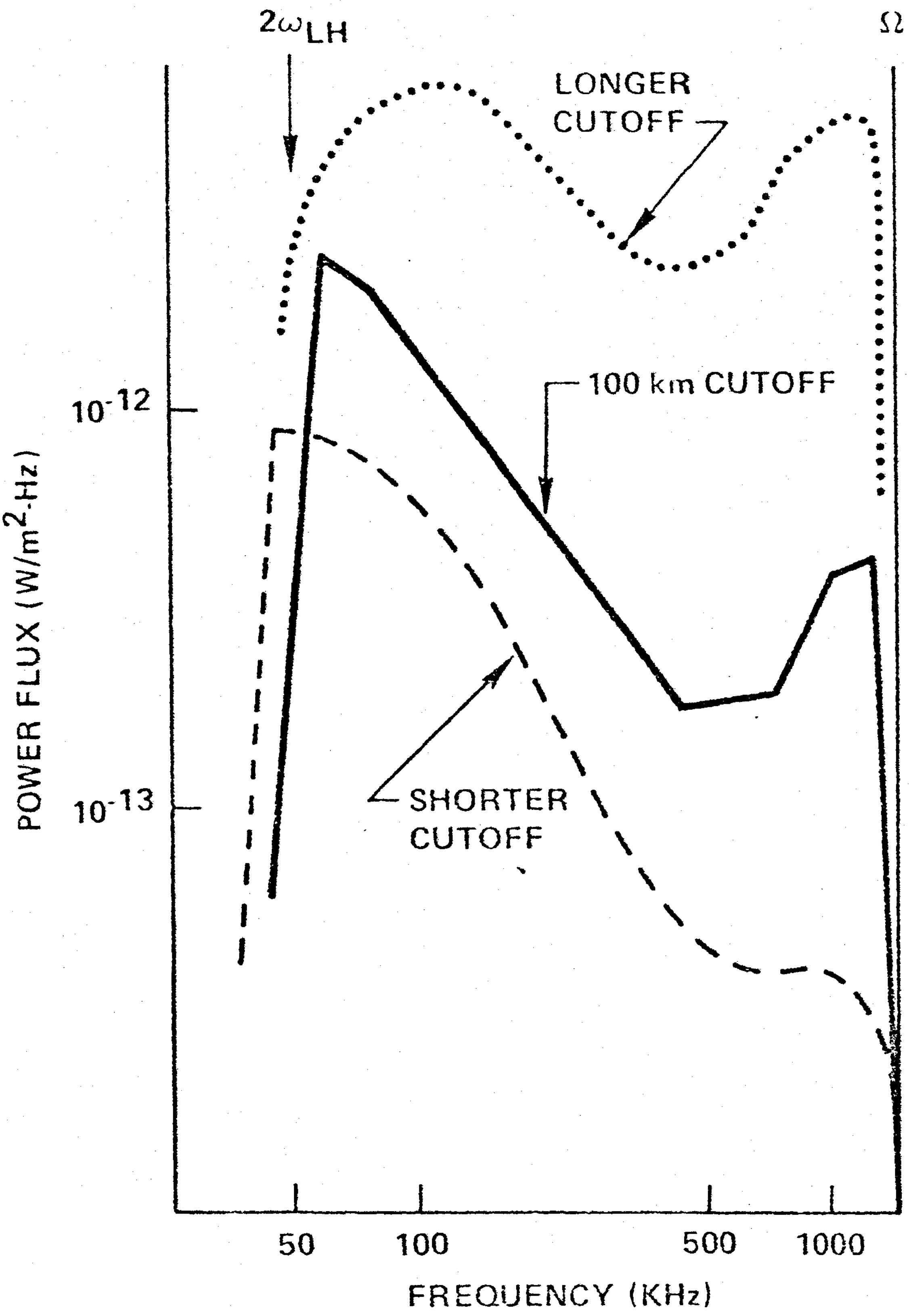

Fig. 6. Power flux spectra predicted by the beam amplifica mechanism at an altitude of 1200 km where $\Pi_- > \Omega_-$. The beam is model 2. The horizontal cutoff distance is 100 km. The spectra longer and shorter cutoff distances are schematic only and illus

FIG. 5. PLOT OF THE RESONANCE FUNCTION $E_{res}/E_{phase} = (1 - n\Omega/\omega)^2$ FOR $n = 0, 1, 2, 3, 4$.
The upper scale is for either model distribution function depicted in Fig. 1. Both have $E_{phase} =$ 3165 eV. This plot indicates the thermal energy of warm and ionospheric electrons which are in resonance with the wave at a given frequency and for a particular cyclotron harmonic.

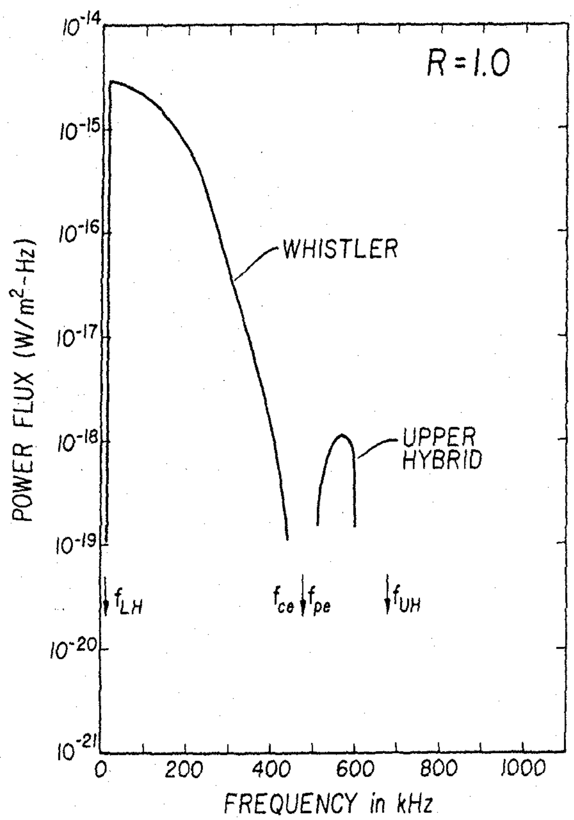

FIG. 6. POWER FLUX FREQUENCY SPECTRUM OF THE WHISTLER AND UPPER HYBRID MODES FOR $R = 1$.
The moderate beam model (Fig. 1) is the source of amplification. The North–South extent of this beam is 1 km. Notice the difference in peak power fluxes of the two modes.

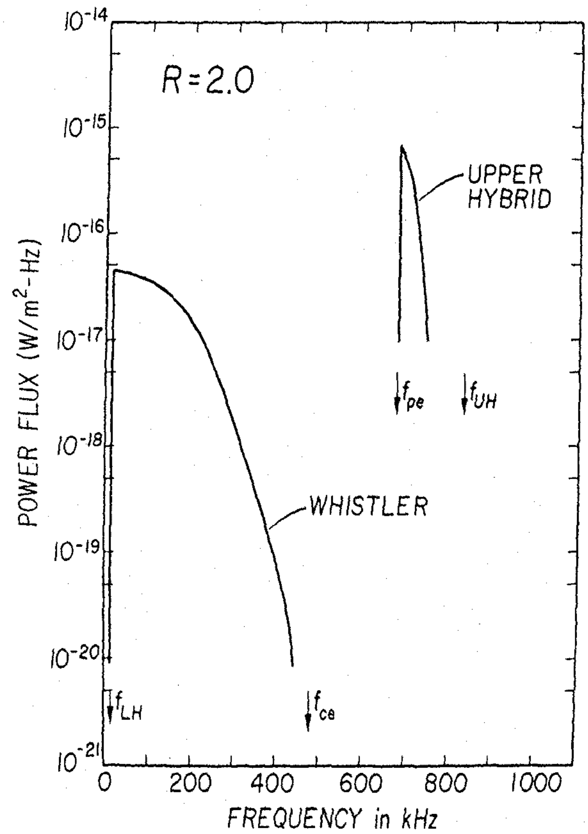

FIG. 7. SAME AS FIG. 6 FOR $R = 2$.
Notice the sharp cutoff of the upper hybrid mode at f_{pe}. Comparison with Fig. 6 shows how the peak power fluxes of the two modes may be used as an indicator of the local R value.

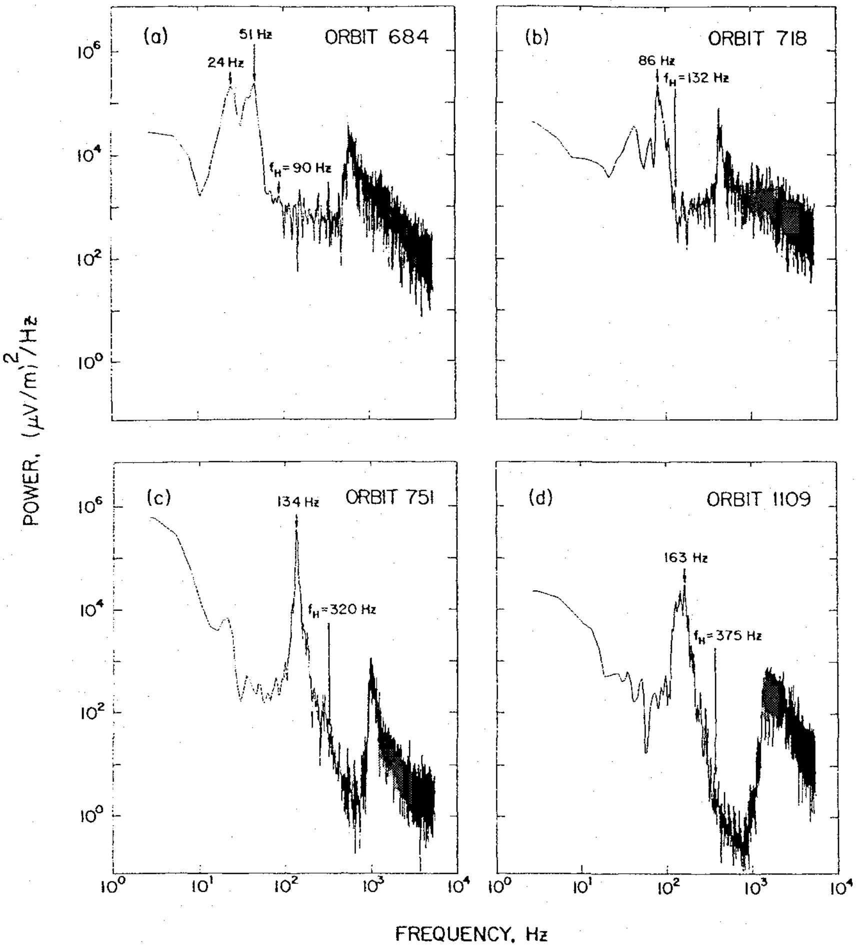

Fig. 6. Power spectra for the examples of narrow-banded ELF waves shown in Figure 5.

For finite $k_\perp$, the two branches couple at the crossover frequency with the result that the whistler branch converts to L polarization at the crossover frequency and as $k_\parallel \to 0$ goes to a frequency above the $L = 0$ cutoff. This cutoff can be observed as the low-frequency cutoff of the plasmaspheric hiss as in some of the examples in Figures 2–4, as well as in the work of *Gurnett and Burns* [1968]. The (L,X) branch approaches the proton gyrofrequency as $k_\parallel \to \infty$ and approaches the ion hybrid frequency [*Buchsbaum*, 1960; *Stix*, 1962] as $k_\parallel \to 0$. For a H^+–He^+ plasma, this frequency is given by

$$\frac{\omega_{IH}}{\Omega_H} = \frac{1}{R}\sqrt{\frac{1+(R-1)C}{1-C(R-1)/R}} \qquad (3)$$

For a mixture of H^+, He^+, and O^+, this frequency is plotted in Figure 8. At very large $k_\perp$ (this is the case under consideration here), these waves become nearly electrostatic at a resonance angle that is nearly 90° for all frequencies except those close to the proton gyrofrequency [*Rauch and Roux*, 1982]. On this resonance cone, the group velocity of the waves becomes closely field-aligned, in contrast to the whistler resonance cone, where the group velocity is oblique, except at the lower hybrid frequency. Therefore, ELF waves should stay on the field line of the source, while VLF waves, as is well known, spread away from the source in a saucer-shaped pattern. This behavior can be seen clearly, for example, in Figure 3*b*.

Since electron beams and sometimes ion conics are observed in the region of these waves, these features are the prime candidates for the source of free energy to drive the waves. To examine this question, it is useful to write the dispersion relation for the waves in the form:

$$Sn_\perp^4 - [S^2 - D^2 + SP - n_\parallel^2 (S+P)]\, n_\perp^2 + P\, [(n_\parallel^2 - S)^2 - D^2] = 0 \qquad (4)$$

where $n_\perp = k_\perp c/\omega$; $n_\parallel = k_\parallel c/\omega$ and S, D, and P are the elements of the cold electromagnetic dielectric tensor as defined by *Stix* [1962]. These elements depend only on ω in the limit of a cold plasma. For an electron or ion with parallel velocity $v_\parallel$ which satisfies the resonance condition at the l^{th} harmonic:

$$\omega - k_\parallel v_\parallel - l\Omega = 0 \qquad (5)$$

the parallel index of refraction is given by

$$n_\parallel = \frac{c}{v_\parallel}\,(1 - \frac{l\Omega}{\omega}) \qquad (6)$$

Thus, given a wave frequency and velocity of resonant particle, the dispersion relation (4) may be solved for $n_\perp$. Such a plot for electrons at the Landau resonance ($l = 0$) is given in Figure 9, assuming $\omega_{pe}/\Omega_e = 0.23$ and

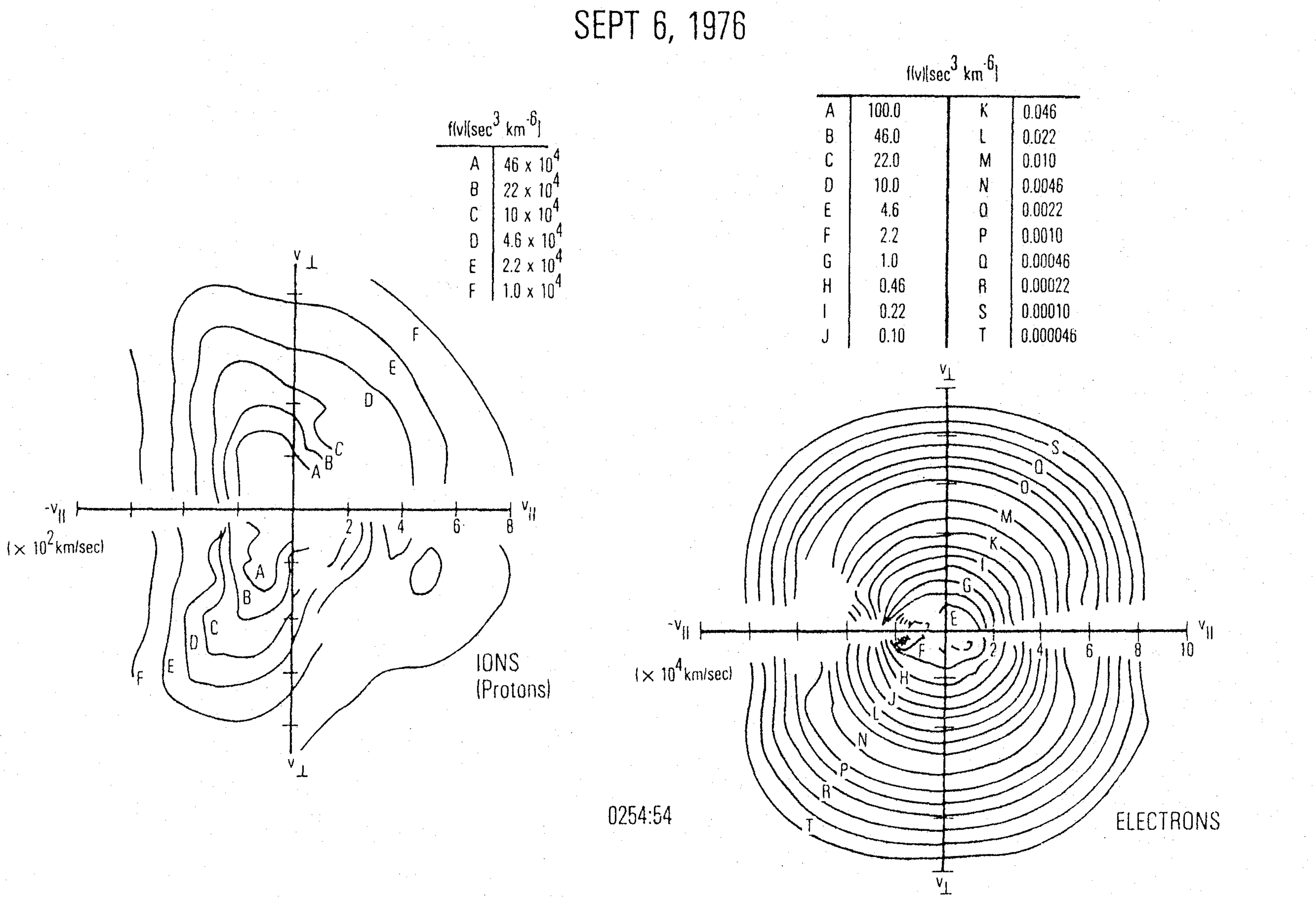

Fig. 5. (*a*) Contour plots of phase space densities of 0.09 to 3.9 keV ions (protons) in velocity space. (*b*) Contour plots of phase space densities of 0.17 to 33 keV electrons in velocity space.

(large $v_{\parallel}$). This is a well-known signature of electrostatic acceleration parallel to B.

The effects of parallel electric fields on ion and electron distributions have been extensively investigated [*Evans*, 1974; *Whipple*, 1977; *Chiu and Schulz*, 1978; *Croley et al*, 1978]. The mapping equations for following the dynamical trajectories of ions in phase space as they move through a potential difference given by Φ and are adiabatically transported in the non-uniform geomagnetic field from a point where $\mathbf{B} = \mathbf{B}_0$ to a

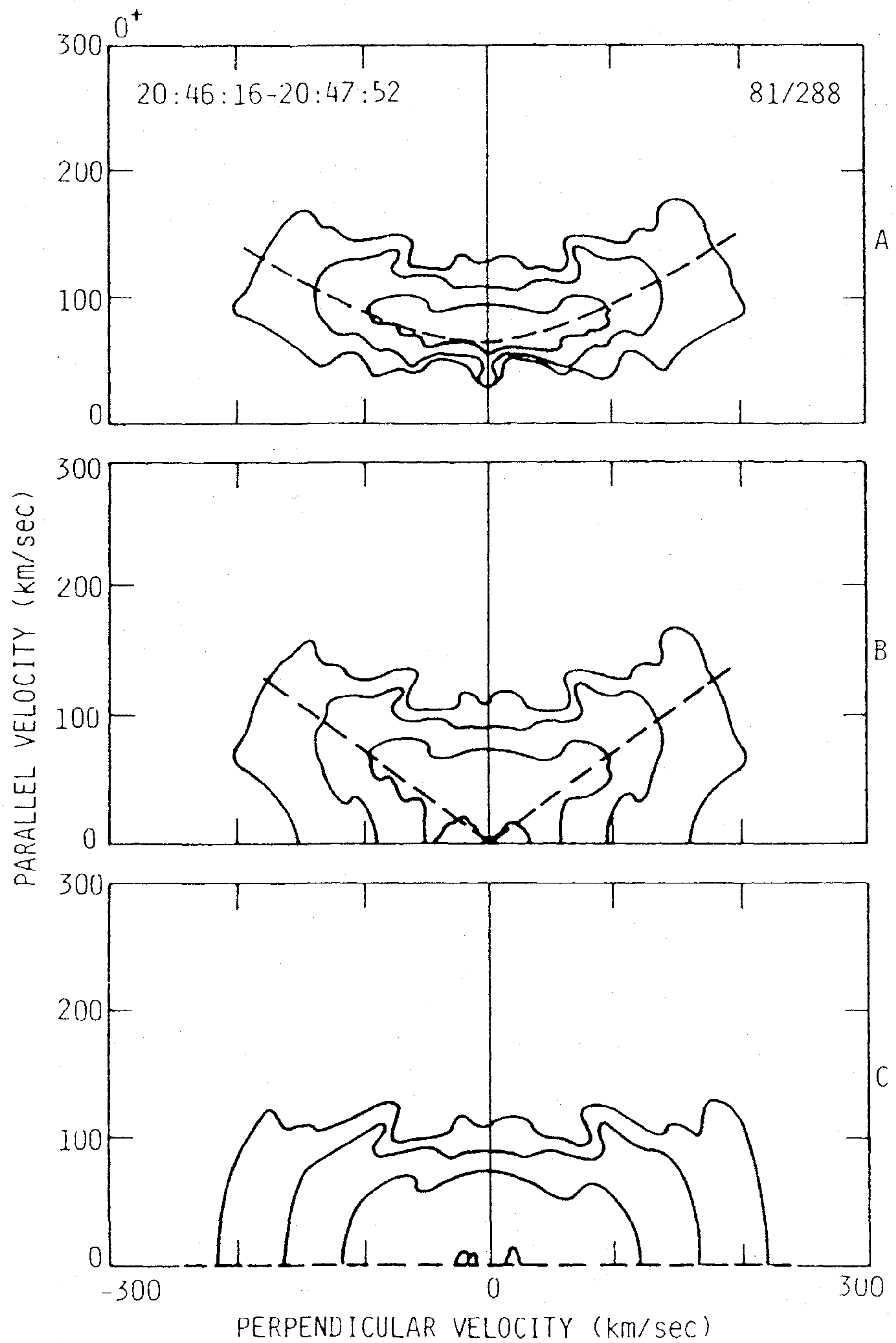

Fig. 3. Phase space density contours at half-decade intervals

$\sqrt{\frac{\text{watts} \times 377}{}}$ $\sqrt{\mu V/m\,Hz^{1/2}}$ $I^2 \ell \sim v^2/R$

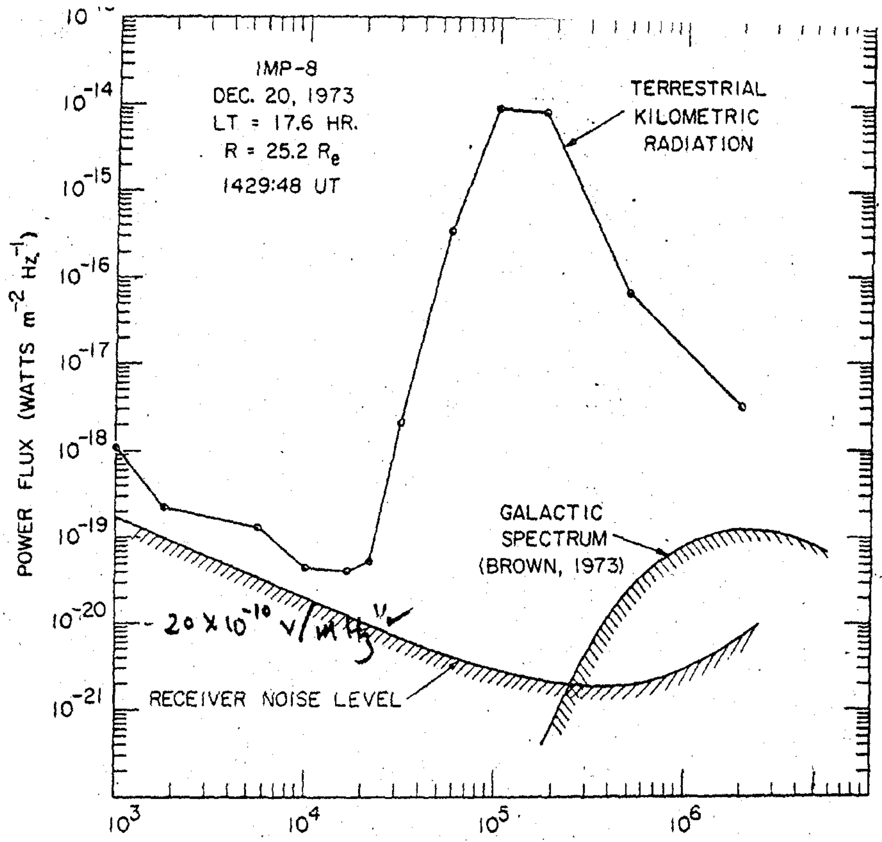

$\sqrt{\frac{4\pi\rho}{c}}$

$\frac{\epsilon E^2}{4\pi}$ $\frac{4\pi}{v_p}$ $\frac{c}{\sqrt{\epsilon}} \frac{\epsilon E^2}{4\pi}$ $\frac{\epsilon\,\epsilon^{1/2} E^2}{4\pi}$ $= \frac{cE^2}{4\pi}\sqrt{\frac{\epsilon_0}{\mu_0}}$

Fig. 3. Power spectrum of terrestrial kilometric radiation as observed by Imp 8 at a radial distance of 25.2 R_E in the local evening.

$\frac{1.2 \times 10^1}{3 \times 10^8}$

of the tip-to-tip length of the antenna and ignoring any antenna impedance corrections. The linear relation between the electric and the magnetic field spectral densities illustrated in the bottom panel of Figure 2 provides convincing evidence that the terrestrial kilometric noise detected by Imp 6 is electromagnetic radiation. The small deviation (~20%) of the electric field amplitude from the $E = cB$ line for electromagnetic waves in free space is believed to be due to the loading effect of the input capacity at the base of the electric antenna. The ab-

terrestrial kilometric radiation indicate that the noise is generated very close to the earth, probably at a radial distance of less than 3 R_E. As was mentioned earlier, the measured intensity of the kilometric noise has a very distinct modulation due to the rotation of the antenna. Figure 4 shows an example

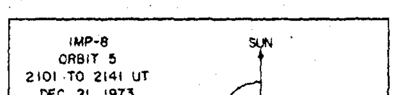

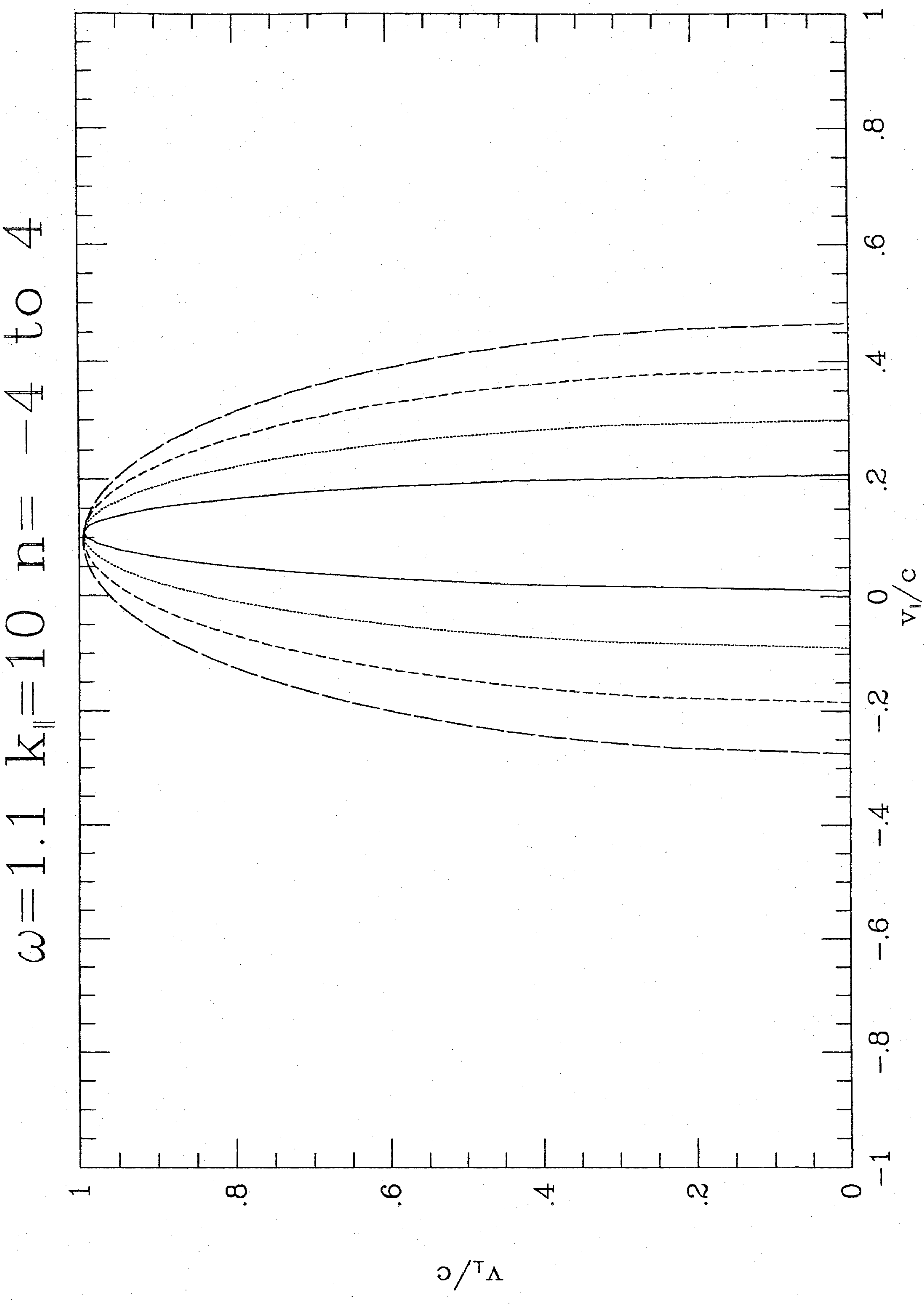

ω=1.1 k∥=10 n= −4 to 4
v∥/c
v⊥/c
−1
−.8
−.6
−.4
−.2
0
.2
.4
.6
.8
1

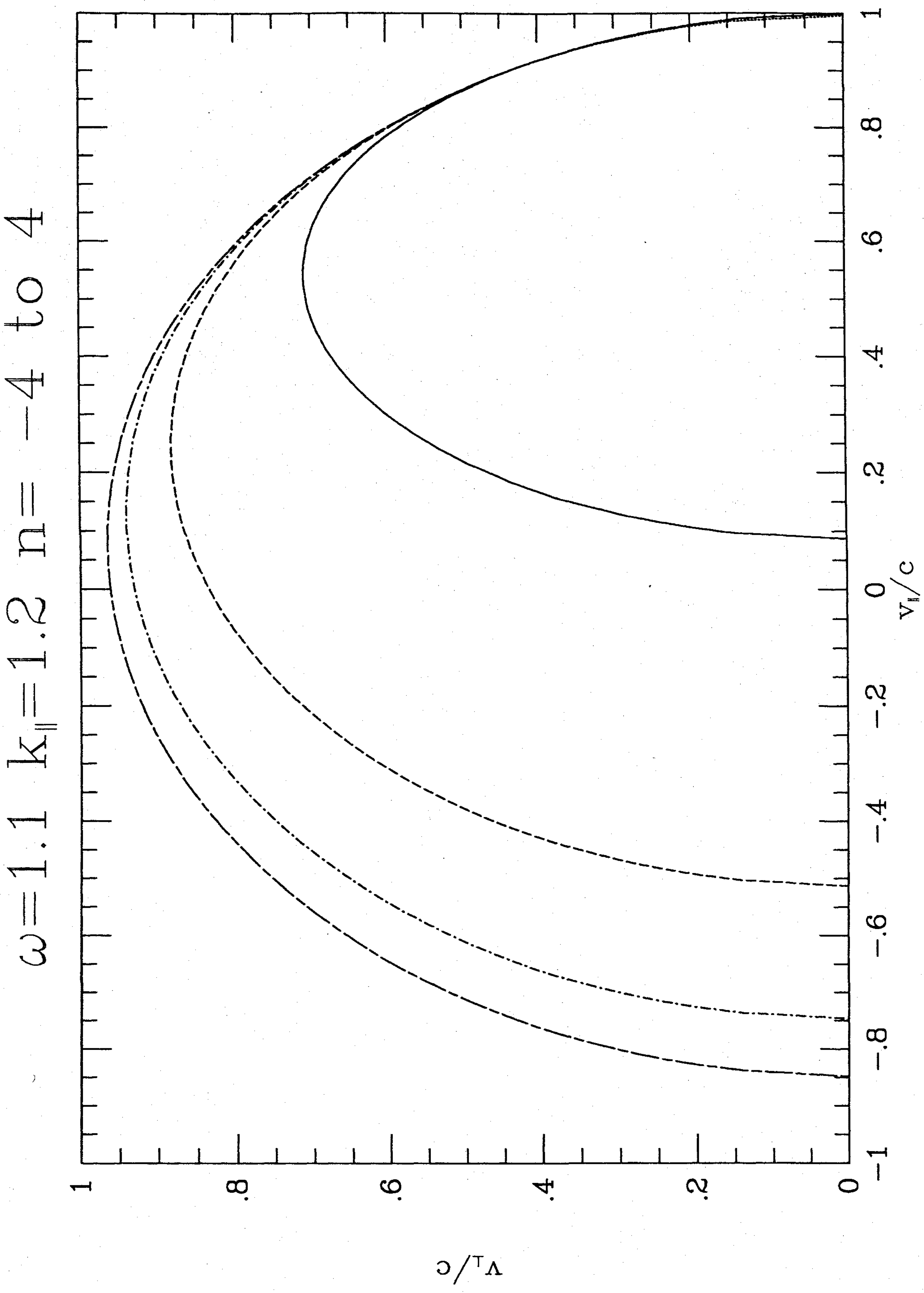
ω=1.1 k∥=1.2 n= −4 to 4
v∥/c
v⊥/c
−1
−.8
−.6
−.4
−.2
0
.2
.4
.6
.8
1
0
.2
.4
.6
.8
1

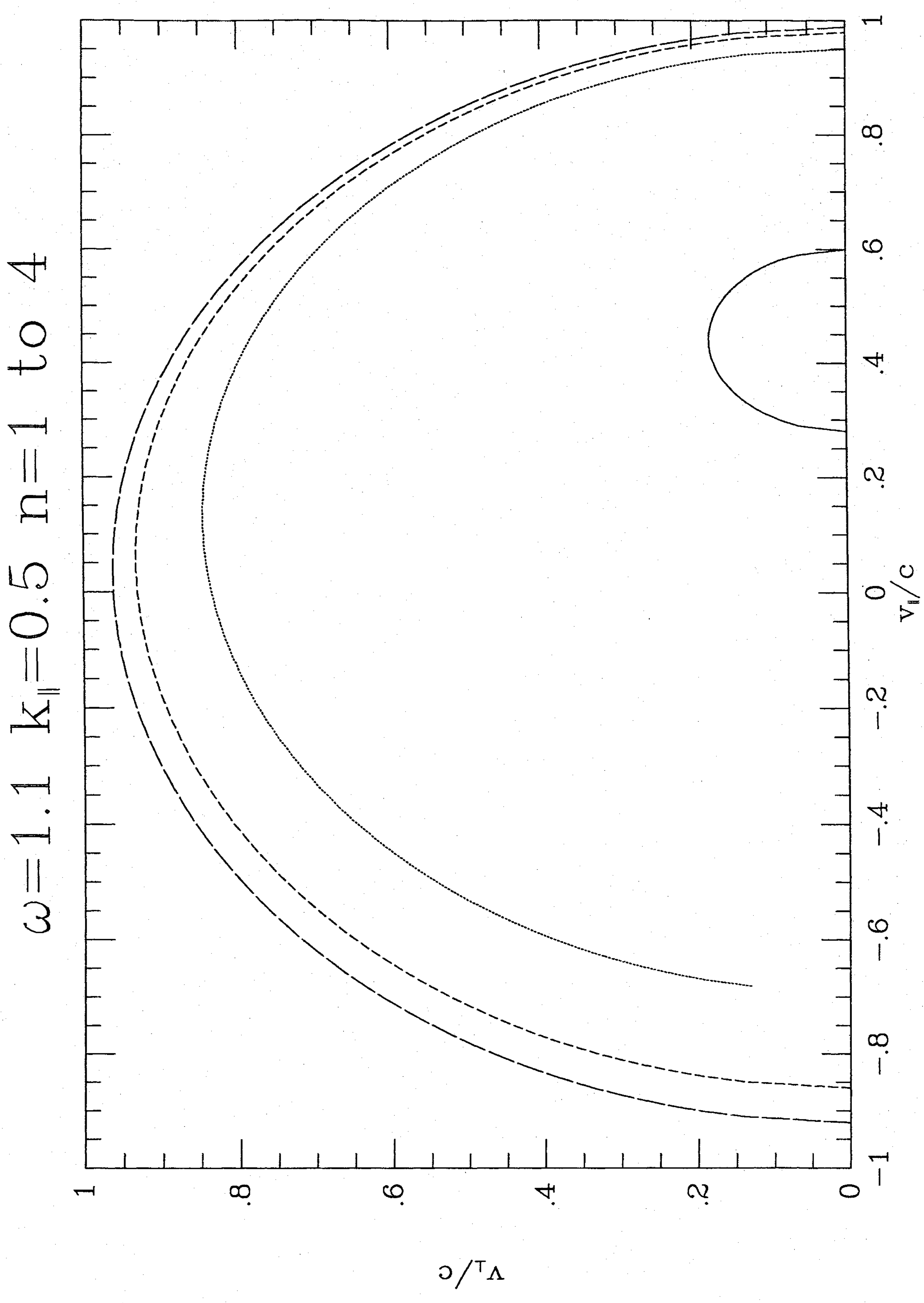

$\omega=1.1$ $k_{\parallel}=0.5$ n=1 to 4
$v_{\parallel}/c$
$v_{\perp}/c$
−1
−.8
−.6
−.4
−.2
0
.2
.4
.6
.8
1

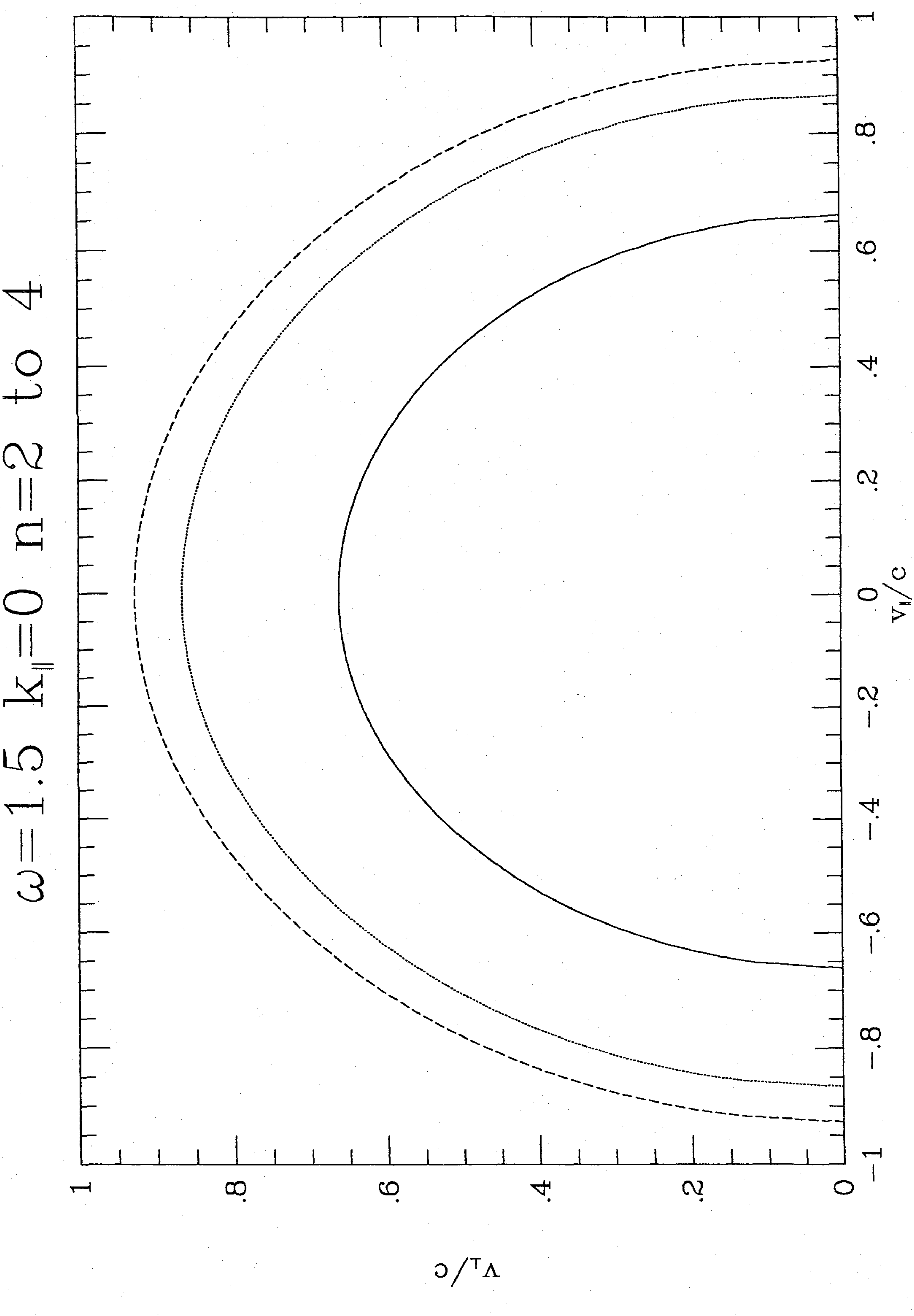

ω=1.5 k∥=0 n=2 to 4
v∥/c
v⊥/c
-1
-.8
-.6
-.4
-.2
0
.2
.4
.6
.8
1
0
.2
.4
.6
.8
1

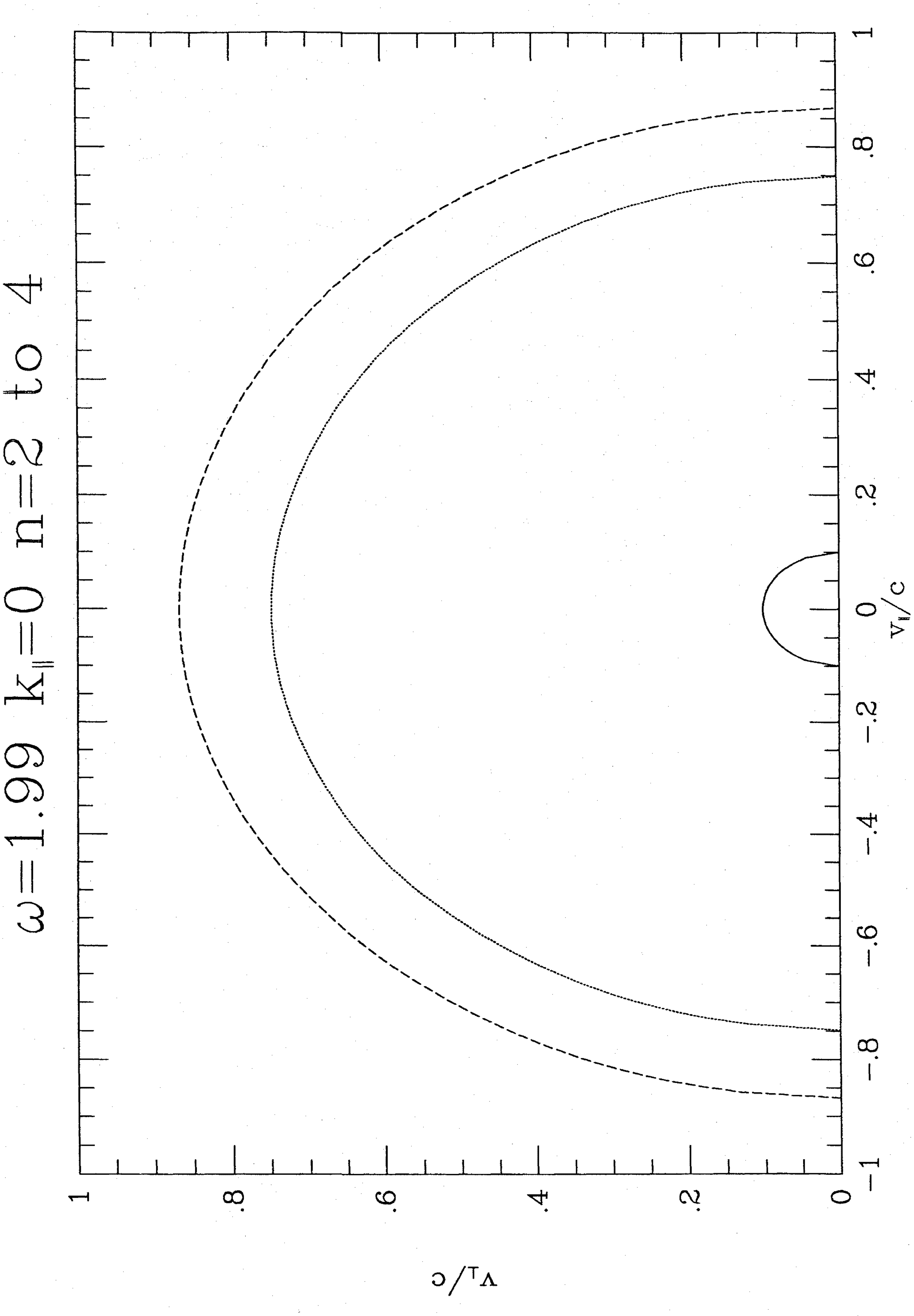

ω=1.99 k∥=0 n=2 to 4
v∥/c
v⊥/c
−1
−.8
−.6
−.4
−.2
0
.2
.4
.6
.8
1
0
.2
.4
.6
.8
1

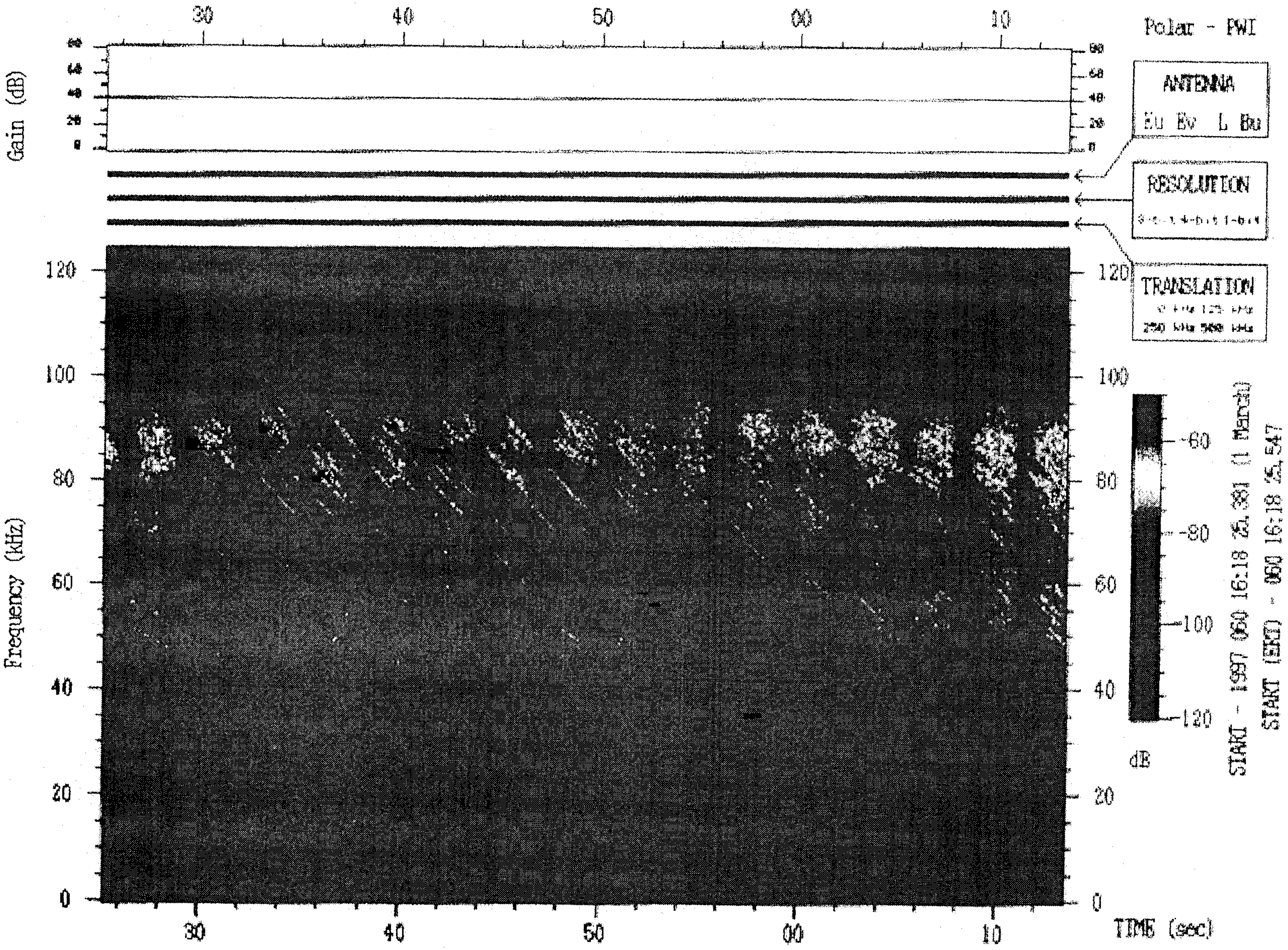

Plate 1. A 48-s frequency-time spectrogram taken from the wideband data for March 1, 1997, starting at 1618:25 UT. At this time the spacecraft is located over the polar cap, well above the auroral kilometric radiation (AKR) source region.

with finite $k_{||}$. This process is simple linear refraction on the R-X branch.

The basic idea is as follows (Fig. 7). The waves, upon reflecting, scatter in angle. If the waves acquire a significant $k_{||}$, they can escape without further reflection. Otherwise, the waves experience more angular scattering. A long, narrow cavity will focus the rays into a beam. The waves

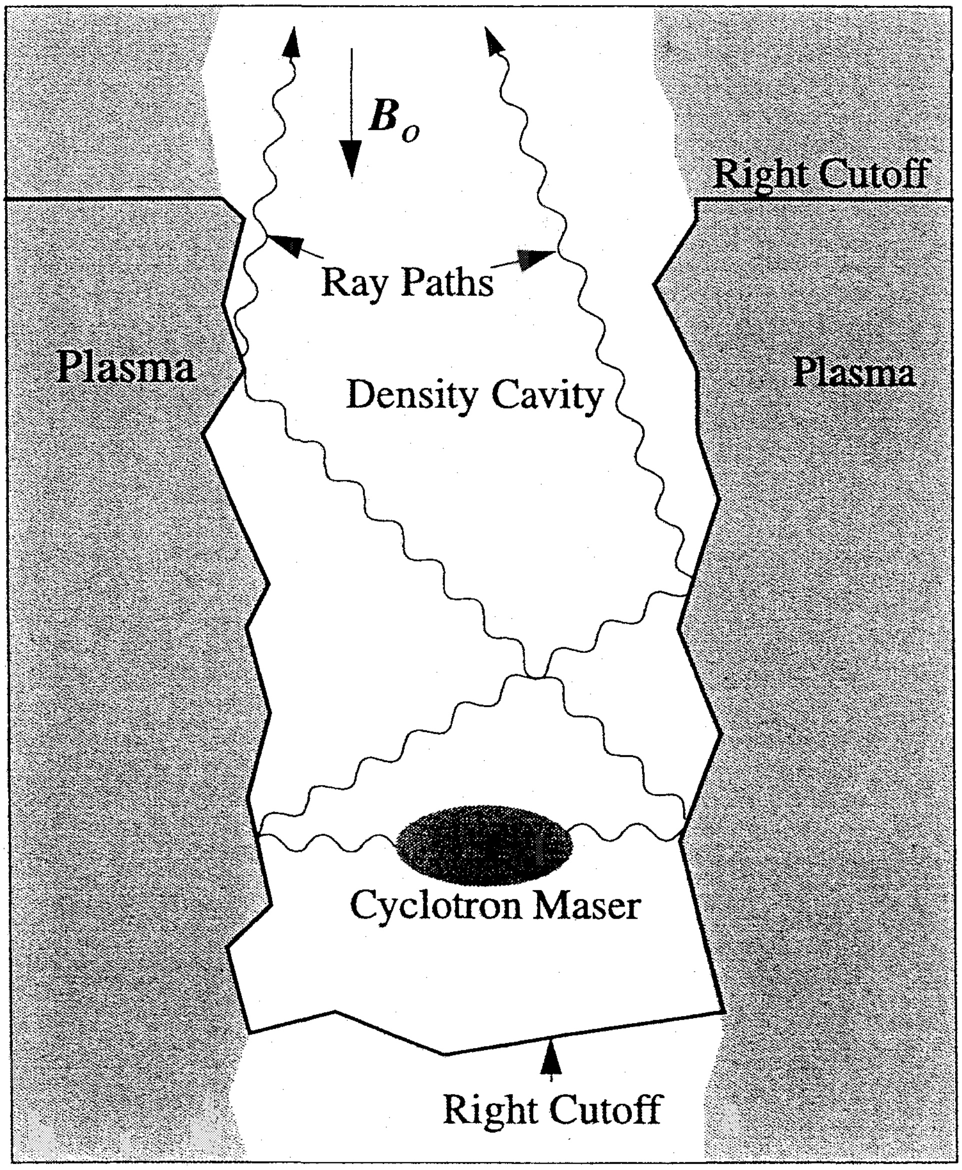

FIG. 7.—Cartoon of the electron-cyclotron maser source region. The radiation propagates at right angles as generated. The rays cannot escape the cavity until they reach weaker magnetic fields (higher altitude) and are above the right cutoff, which requires reflection at the boundaries of the cavity. The cavity can guide the waves and efficiently convert the radiation to more parallel propagating R-X mode. This process is observed for AKR.

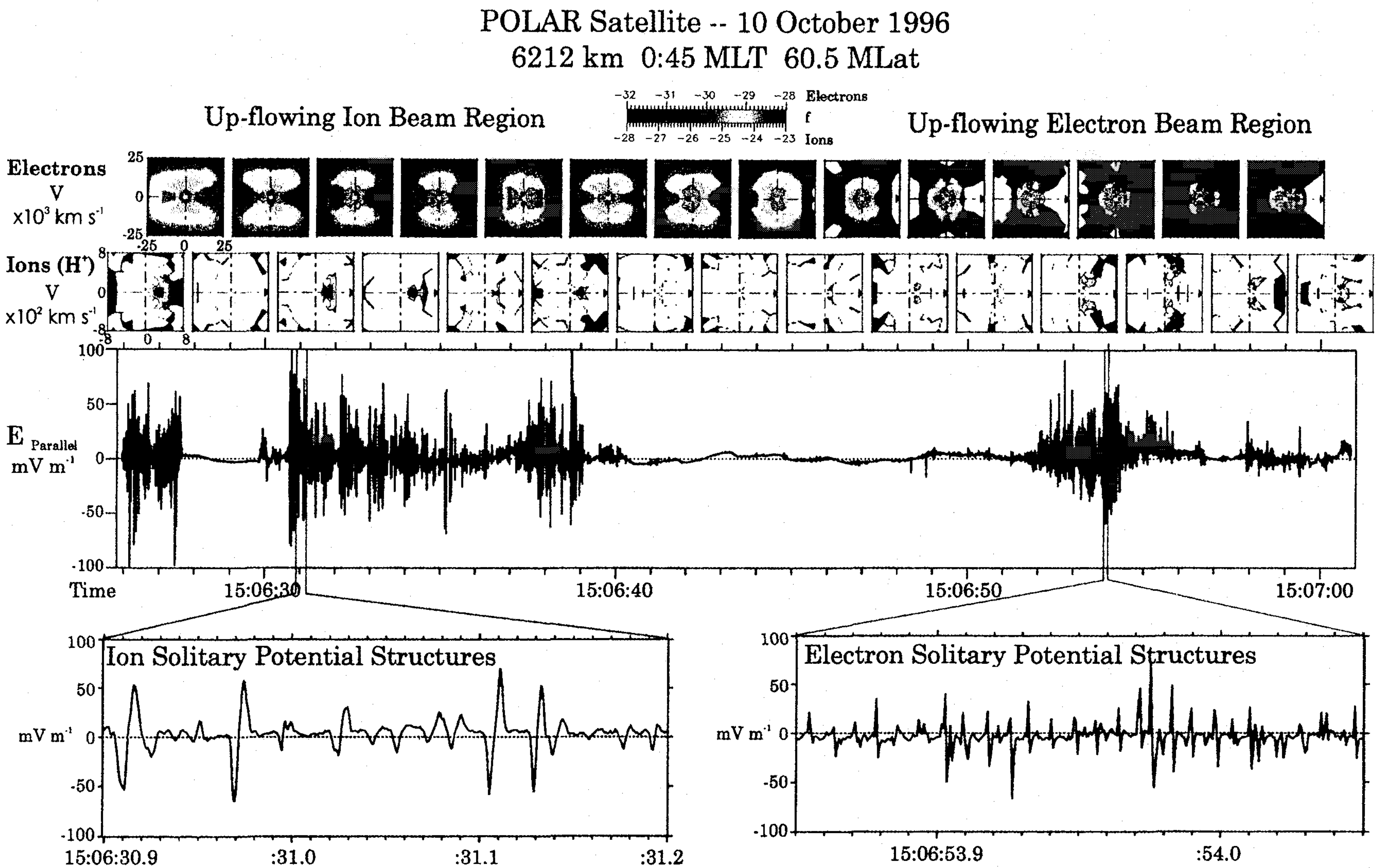

Plate 2. Time evolution of the ion and electron particle distributions with respect to contiguous observations of the parallel electric fields which include ion and electron solitary potential structures on October 10, 1996. The strong correlation of solitary potential structures and upflowing ion beams can clearly be seen in the first half of the data. In the ion solitary potential structure region, electrons display a loss cone type distribution and the ions display a strong anti-earthward parallel acceleration. The second half shows the distributions in a region of electron solitary potential structures. Here the total electron population is colder and does not show distinct loss cone features, whereas the ions show conic distributions. The electrons show anti-earthward directed beams accelerated parallel to the magnetic field.

Formation of weak double layers by FAC
(Observations: S3-3, Viking)

- WDL are coherent nonlinear state of ion acoustic (??) turbulence

- Electron drift can amplify negative potential fluctuations

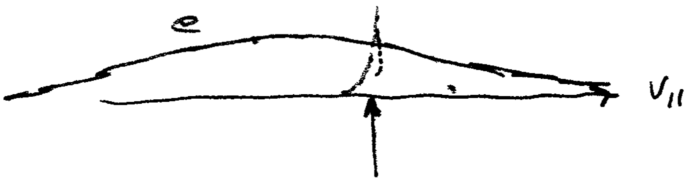

- Consider "hole" in ion distribution

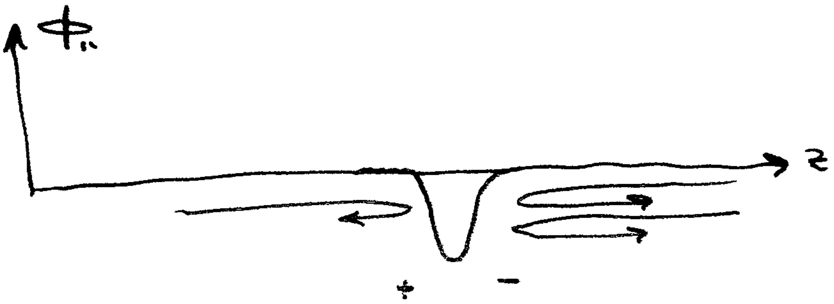

- More electrons reflected on right side than left ⟹ space charge buildup

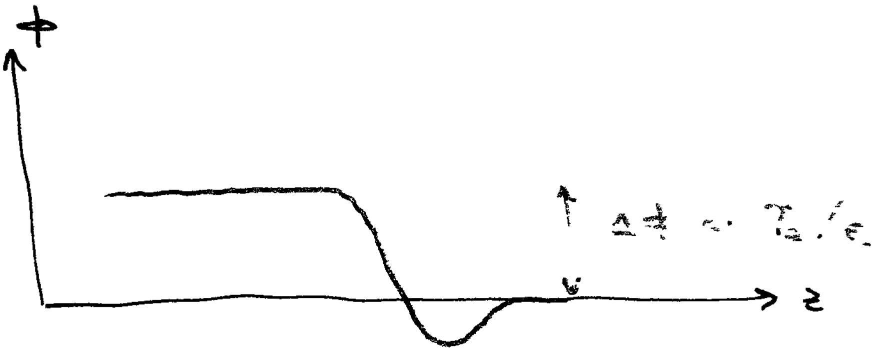

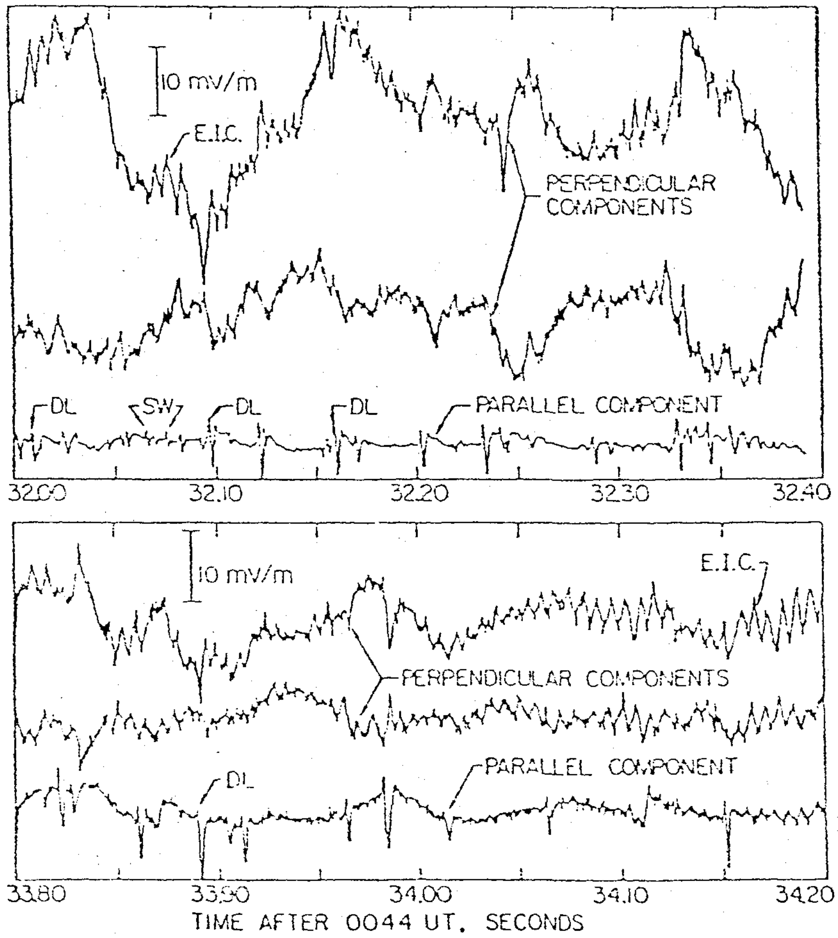
10 mv/m
E.I.C.
PERPENDICULAR COMPONENTS
DL
SW
DL
DL
PARALLEL COMPONENT
32.00
32.10
32.20
32.30
32.40
10 mv/m
E.I.C.
PERPENDICULAR COMPONENTS
DL
PARALLEL COMPONENT
33.80
33.90
34.00
34.10
34.20
TIME AFTER 0044 UT, SECONDS

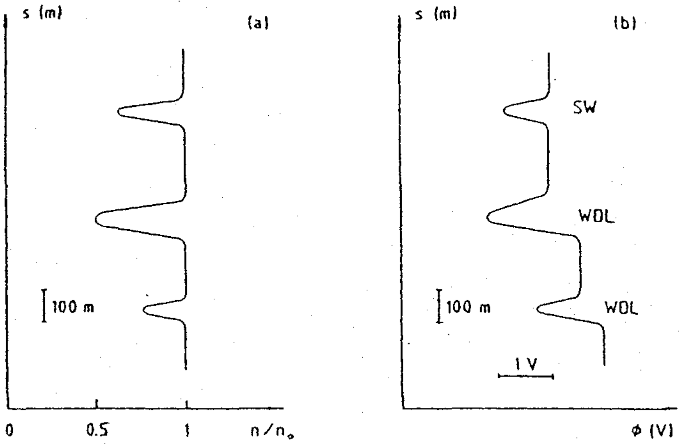

Fig 1.

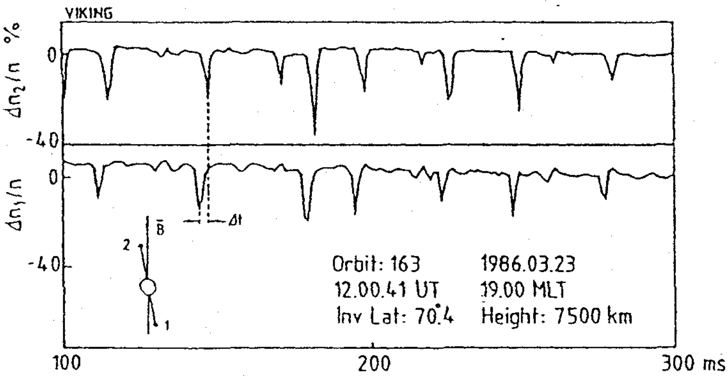

Fig 2.

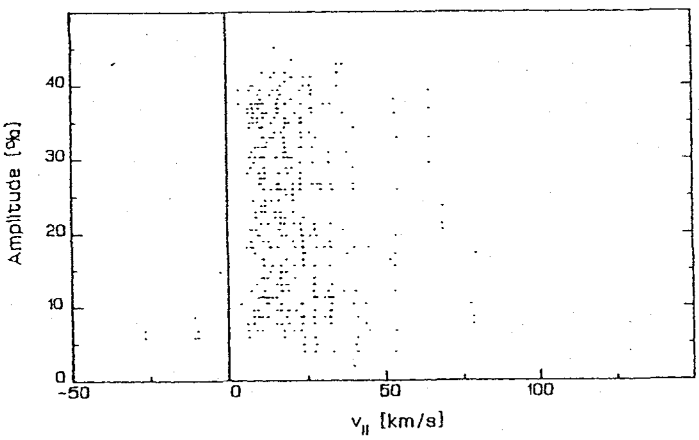

Fig 3.

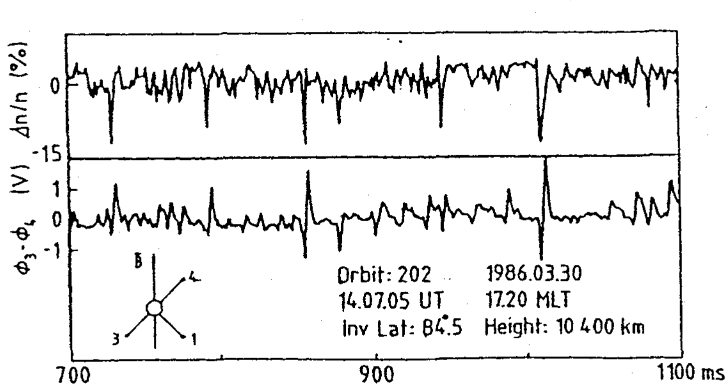

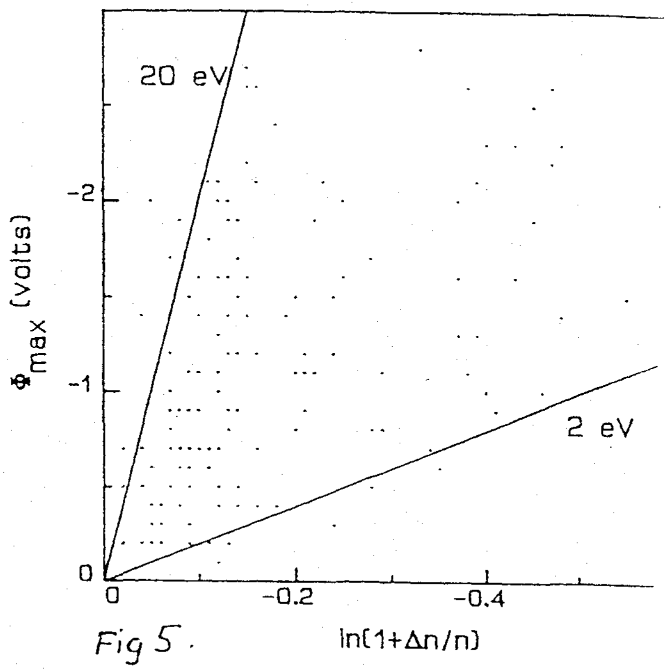

Fig 5.

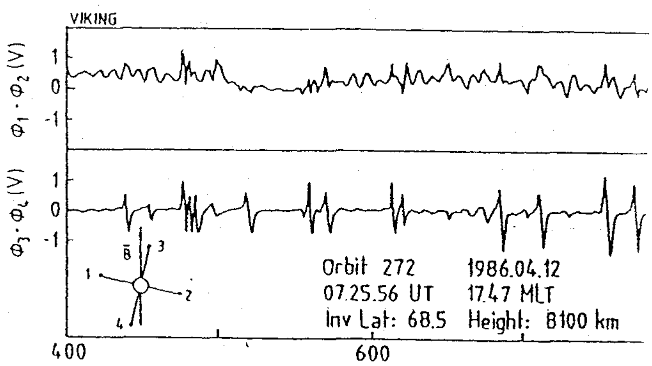

Fig 6.

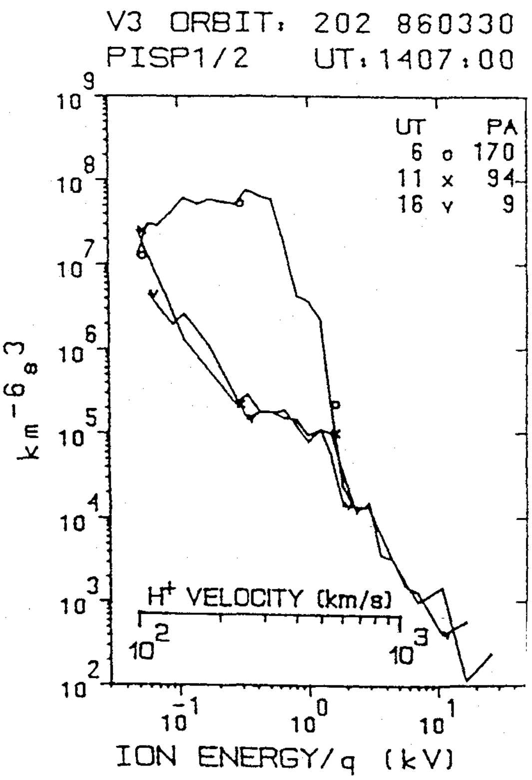

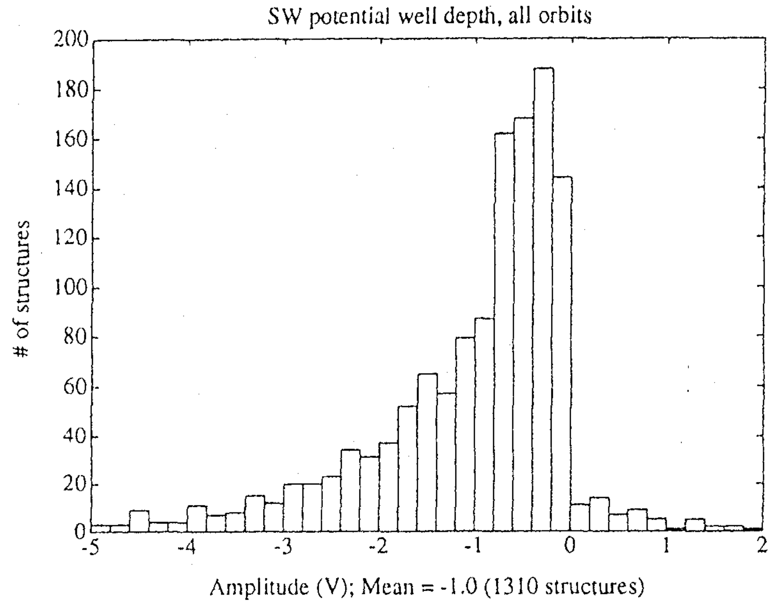

Fig. 6. Solitary wave potential well depths. The SWs have consistently negative potentials, and the mean value for all measured well depths is -1.0 V.

all SWs move upwards. Statistics from the interferometric measurements in the NN mode (to be discussed in more detail in paper 3) show that a few SWs possibly are moving downwards, and thus the signatures of positive potential amplitudes may be due to downward-moving structures. As a consequence, we state that we have observed potential dips with consistently negative potentials and with a mean potential well depth of -1 V.

In Figure 7 we have plotted the measured net potential drops as a function of altitude on a grey scale plot. Positive sign corresponds to higher potential at higher altitude along the field line and the grey levels are on a linear scale from white to black, black corresponding to highest occurrence frequency. The figure shows some interesting features. First, there is a clear preference altitude between 7000 and 11,000 km where most of the SWs are seen. The distribution

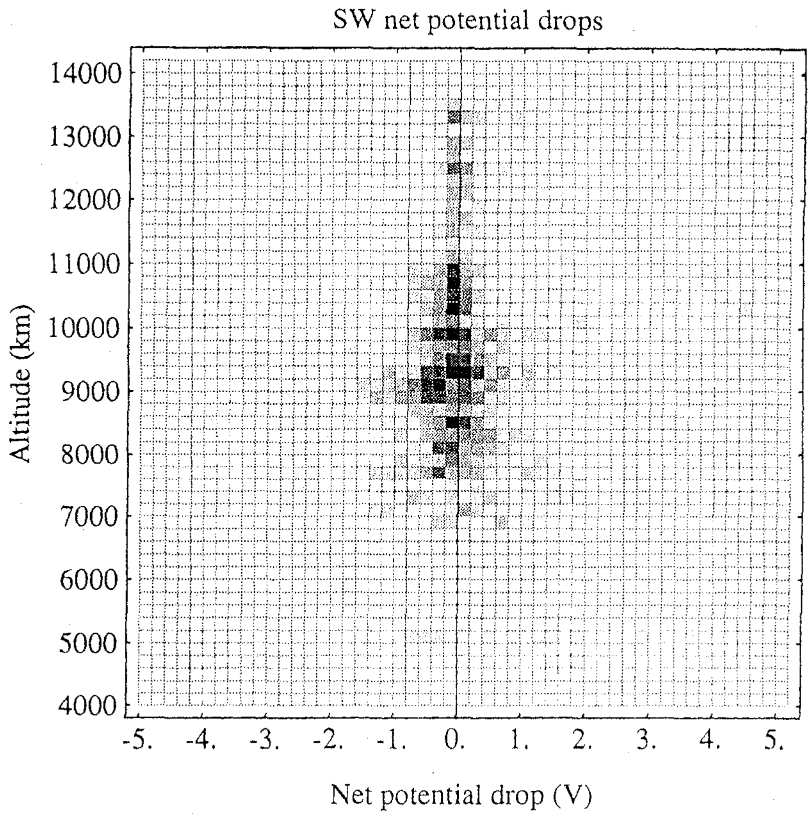

Fig. 7. Solitary wave net potential drops as a function of altitude. The highest occurrence frequency corresponds to black, zero to white and the color scale is linear. The highest occurrence frequencies are in bins closest to zero net potential drop but, at the same time, the height-integrated probability of measuring a solitary wave with a negative net potential drop is approximately twice that of measuring a positive net potential drop. Note also that in this figure we have included all data from different regions of the auroral oval and thus the physical conditions may vary considerably between measurements on different orbits. On individual orbits the mean value for measured net potential drops varies between -0.6 and $+0.1$ V.

two consecutive structures with the same polarity should be $0.58^2 + 0.42^2 = 0.51$. If we put these 768 structures together in chronological order, we find that the actual probability of having the same sign in the polarity for two consecutively

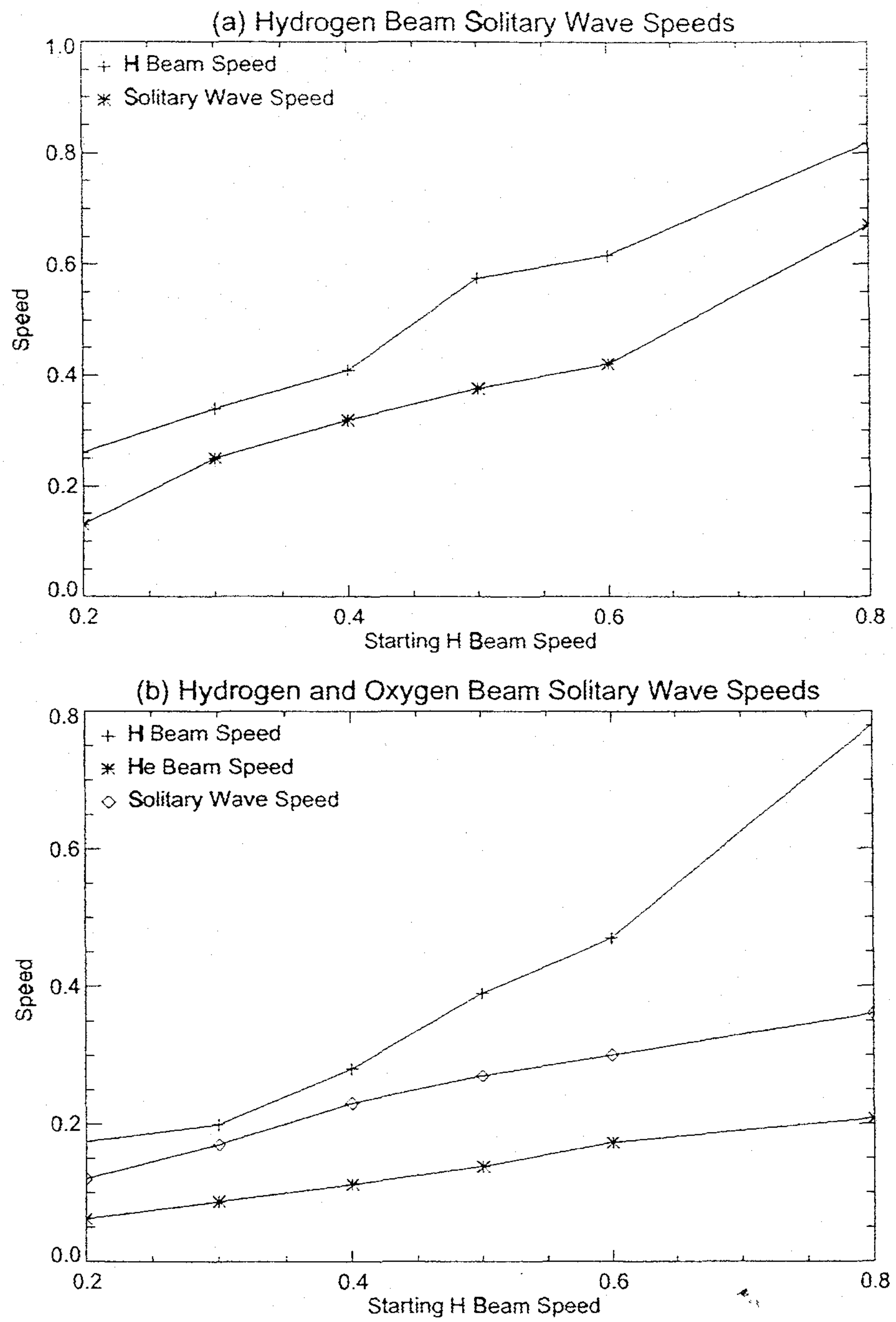

lots show solitary waves speeds and beam speeds at the time of the measured rsus starting hydrogen beam speed for (a) hydrogen beam only runs and (b) ygen beam runs. All speeds are normalized to the starting electron thermal

;rongly depleted around $x = 0$ where the solitary po-
ential is centered, and flat-topped for positions away
'om it. Note also how F bulges where the potential
; large. This feature translates into a brief broaden-
ıg of electron distributions observed in the spacecraft
'ame when a potential spike passes by. Because the
rift speed is a fraction of the velocity spread, this may
:sult in a reverse flux of energetic electrons being ob-
:rved in the spacecraft frame, as seen in the FAST
ataset.

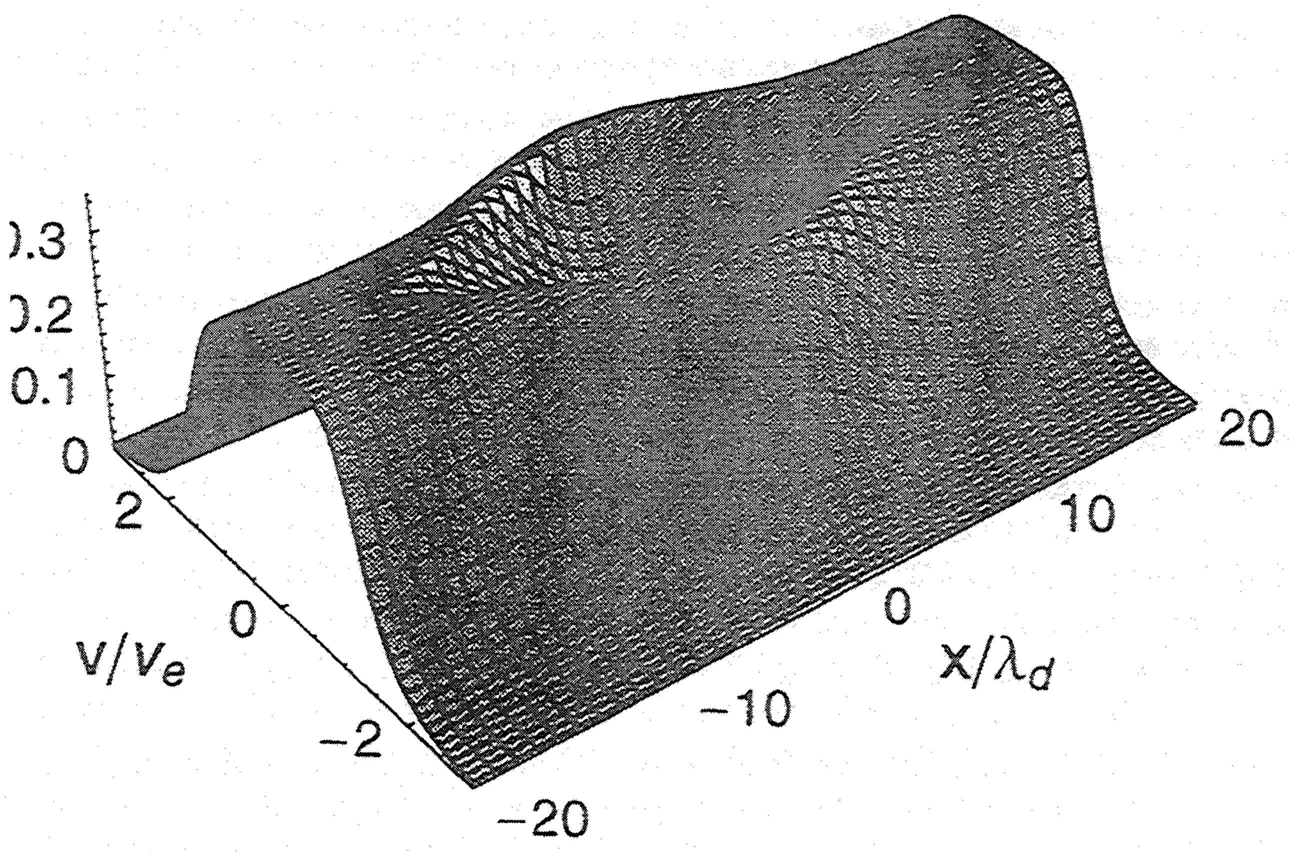

gure 1. Distribution function in (x, v) space exhibit-
; an electron hole. Perspective view made from (6)
th $w = v^2 - \phi(x)$. The associated potential is cen-
:ed on $x = 0$ with a width $\delta = 5\ \lambda_d$. As a function
v, the flat-top distribution bulges and becomes core
pleted at the potential spike.

measurement, which is approximately a factor of two. The large uncertainty in velocity observations has two effects. First, it tends to reduce the curvature in the relation as predicted by (7). Next, since the velocity is derived from the inverse of delay time, a large uncertainty results in a net change in the statistical mean. Properly accounting for this uncertainty in the observations is very difficult. Instead, we modify the expected relationship as predicted by (7) for the large uncertainty in delay times, which yields the light dashed line. One can see that the observations quantitatively agree with the predicted size amplitude relation of a one-dimensional BGK structure.

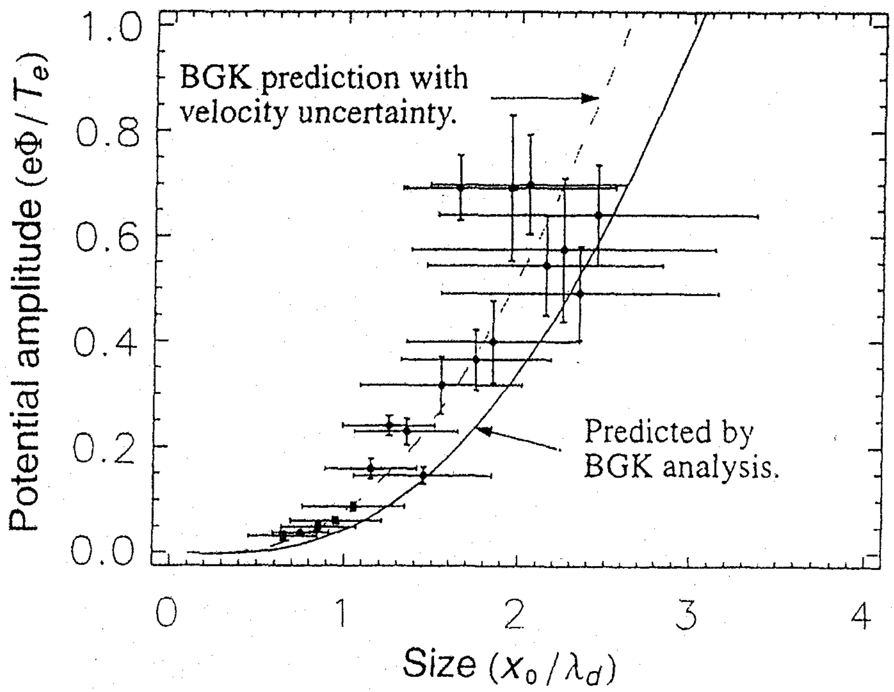

Figure 2. Width-amplitude relation. Statistical determination from the FAST dataset vs prediction for a BGK electron hole. See text for details.

This keeps the noise level low, allows for good diagnostic, and is essential to produce a smooth injection at the boundaries. Typically, we load 2^{10} particles per Debye square at $t = 0$. Their total number in the system is allowed to fluctuate in time via realistic losses and gains through the boundaries; the resulting potential fluctua-

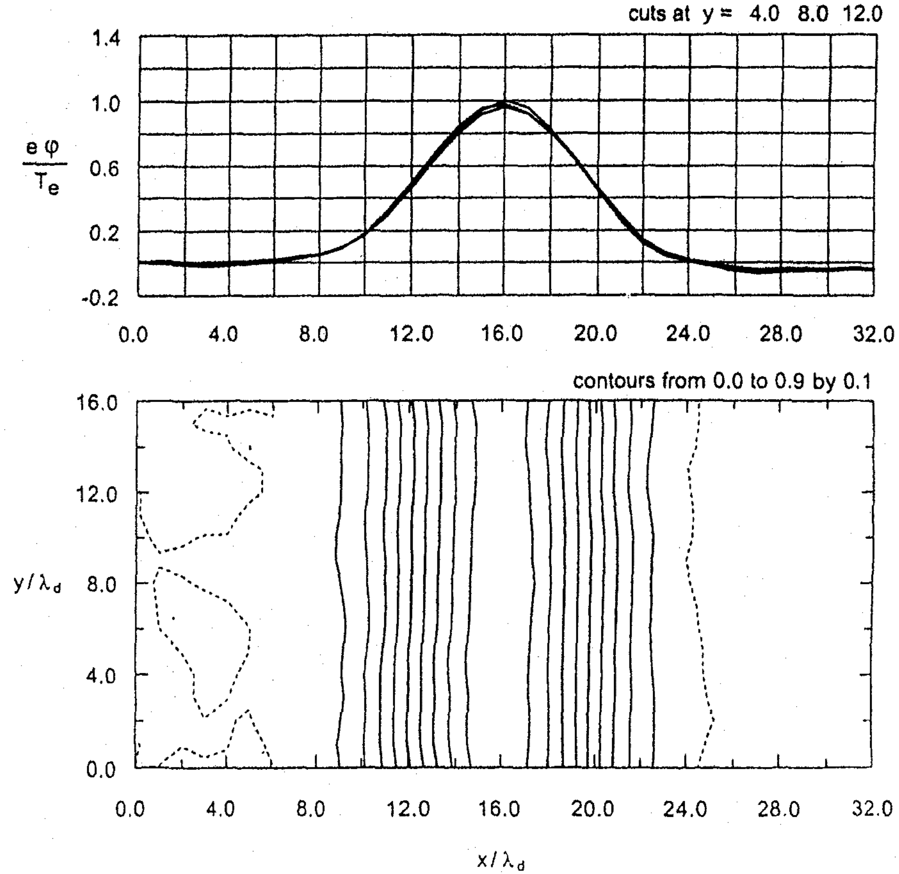

Figure 3. Typical potential structure recorded during the 2-D PIC simulations. (Bottom) Ten contours in (x, y) plane from 0.0 (dotted) to 0.9. (Top) Three cuts at various y, the coordinate perpendicular to the magnetic field. Except for small fluctuations, the potential spike maintains its one dimensional character and is very stable.

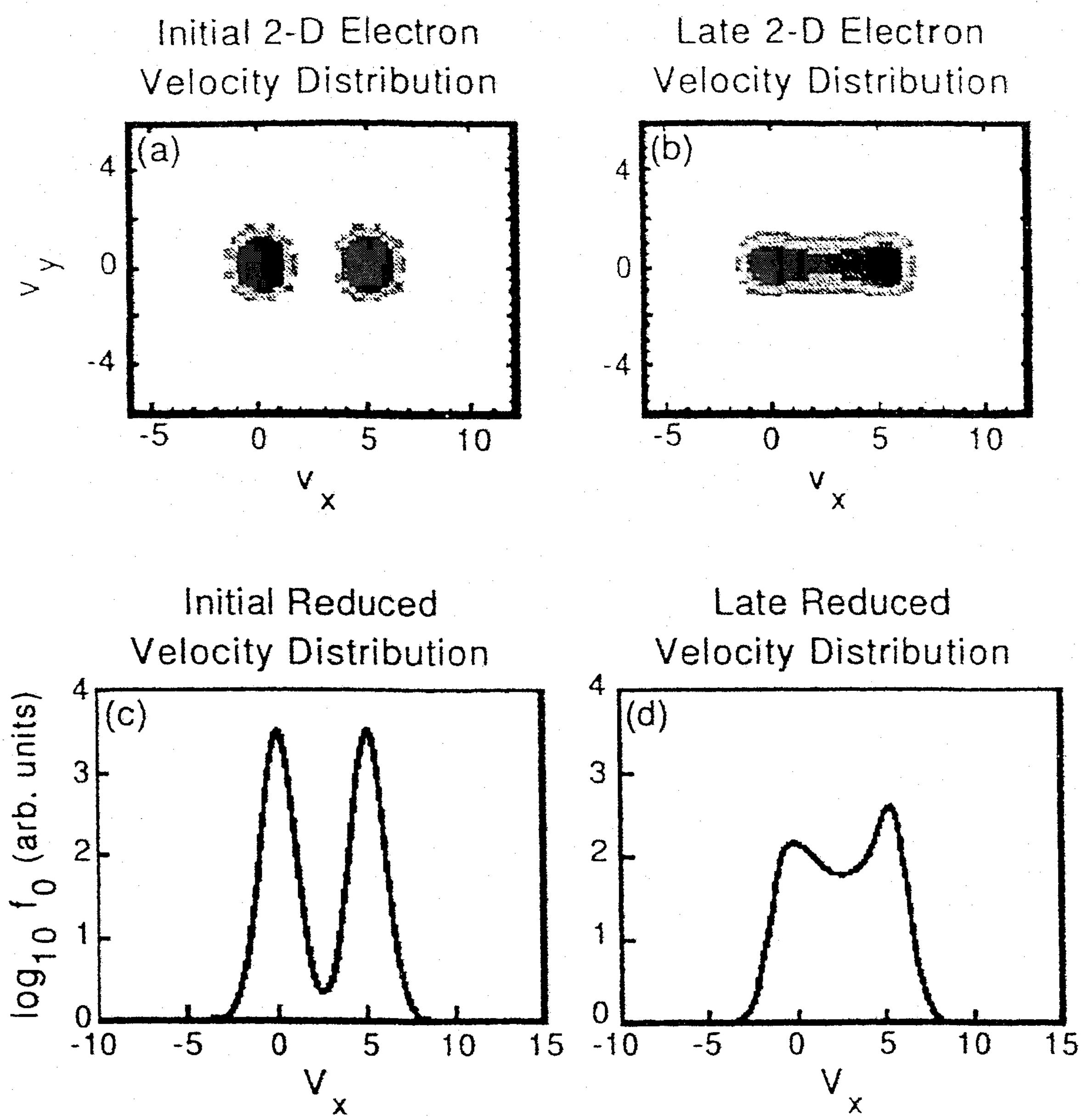

Figure 1. Evolution of space-averaged electron velocity distribution in units of initial rms velocity-width of one of the beams. Figs. 1a and 1b are initial and late-time plots of distribution in v_x–v_y space. Figs. 1c and 1d are initial and late-time plots of reduced distribution function (integrated over v_y).

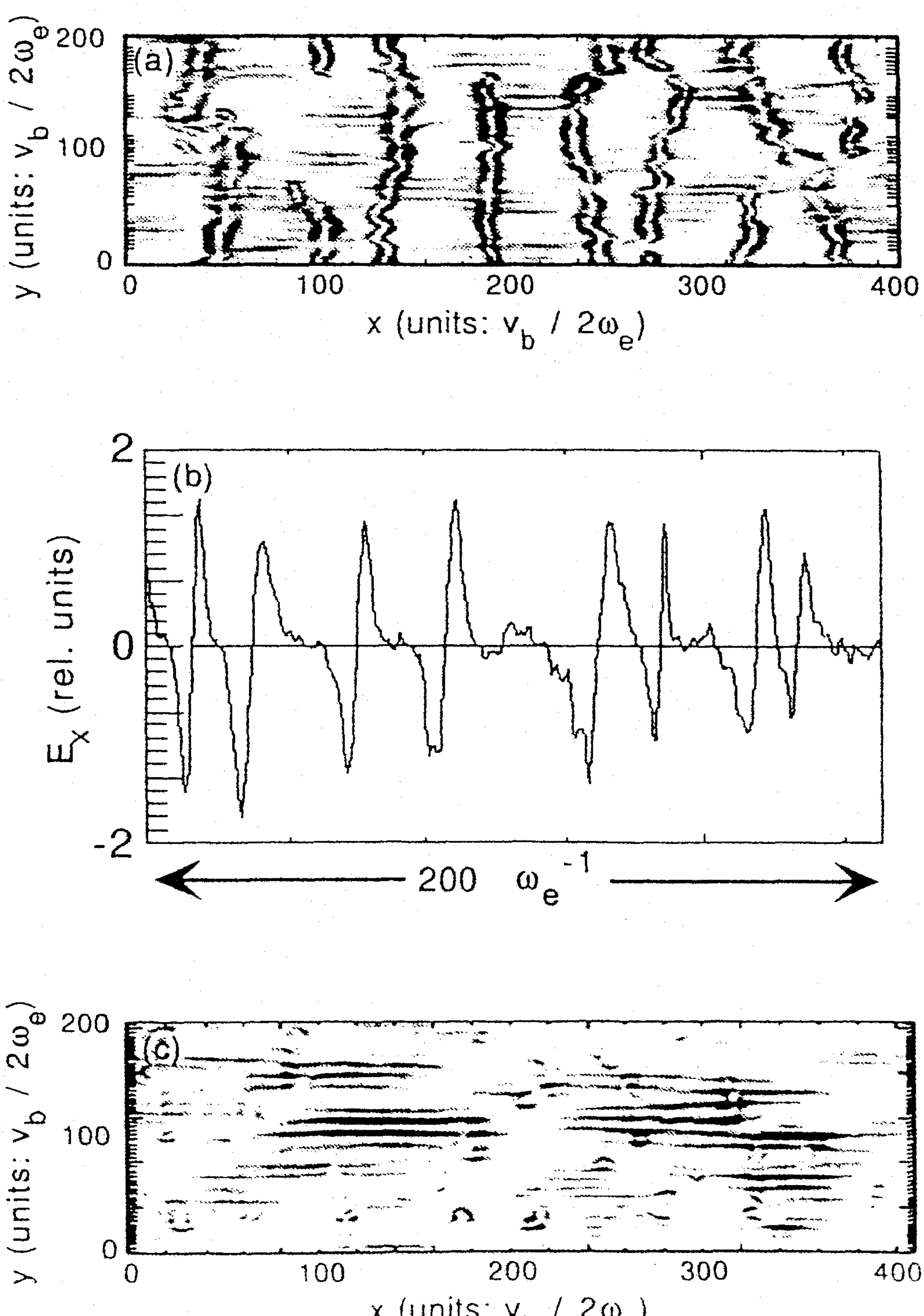

Figure 2. Wave electric field structures in 2-D. (a) detail of $|\mathbf{E}(x, y^2)|$ at early time showing bipolar structures and low-level whistlers. (b) time history of E_x at a fixed spatial point. (c) $|\mathbf{E}(x, y)^2|$ at late, whistler-dominated time.